ScRNA-seq of Diverse Pheochromocytoma Patients Reveals Distinct Microenvironment Characteristics and Supports an Informative Molecular Classification System

Sen Qin[1*], Yawei Xu[1*], Shimiao Yu[1], Wencong Han[1], Shiheng Fan[2], Wenxiang Ai[2], Kenan Zhang[1], Yizhou Wang[1], Xuehong Zhou[1], Qi Shen[1], Kan Gong[1#], Luyang Sun[1#], Zheng Zhang[1#]

[1]Department of Biochemistry and Molecular Biology, School of Basic Medical Sciences, Department of Urology, Peking University First Hospital, Peking University Health Science Center, Beijing 100191, China;

[2]Shenzhen Institute of Ladder for Cancer Research, Shenzhen 518020, China.

[*]These authors contributed equally

[#]Correspondence: Zheng Zhang, M.D.; Kan Gong, M.D.; Luyang Sun, Ph.D.

Email: doczhz@aliyun.com; gongkan_pku@126.com; luyang_sun@hsc.pku.edu.cn

ABSTRACT

Pheochromocytomas (PCCs) are rare neuroendocrine tumors that originate from chromaffin cells in the adrenal gland. However, the cellular molecular characteristics and immune microenvironment of PCCs are incompletely understood. Here, we performed single-cell RNA sequencing (scRNA-seq) on 16 tissues from 4 sporadic unclassified PCC patients and 1 hereditary PCC patient with Von Hippel-Lindau (VHL) syndrome. We found that intra-tumoral heterogeneity was less extensive than the inter-individual heterogeneity of PCCs. Further, the unclassified PCC patients were divided into two types, metabolism-type (marked by NDUFA4L2 and COX4I2) and kinase-type (marked by RET and PNMT), validated by immunohistochemical staining. Trajectory analysis of tumor evolution revealed that metabolism-type PCC cells display phenotype of consistently active metabolism and increased metastasis potential, while kinase-type PCC cells showed decreased epinephrine synthesis and neuron-like phenotypes. Cell-cell communication analysis showed activation of the annexin pathway and a strong inflammation reaction in metabolism-type PCCs and activation of FGF signaling in the kinase-type PCC. Although multispectral immunofluorescence staining showed a lack of $CD8^+$ T cell infiltration in both metabolism-type and kinase-type PCCs, only the kinase-type PCC exhibited downregulation of *HLA-I* molecules that possibly regulated by *RET*, suggesting the potential of combined therapy with kinase inhibitors and immunotherapy for kinase-type PCCs; in contrast, the application of immunotherapy to metabolism-type PCCs (with antigen presentation ability) is likely unsuitable. Our study presents a single-cell transcriptomics-based molecular

classification and microenvironment characterization of PCCs, providing clues for potential therapeutic strategies to treat PCCs.

INTRODUCTION

Pheochromocytomas (PCCs) are rare neuroendocrine tumors that originate from chromaffin cells in the adrenal gland (Fishbein *et al*, 2017; Liu *et al*, 2018; Nölting *et al*, 2022). PCCs have been shown to display a remarkable diversity of driver alterations, including germline and somatic mutations as well as somatic fusion genes (Favier *et al*, 2015; Pillai *et al*, 2017; Toledo *et al*, 2017). This diversity is reflected in the current molecular taxonomy of PCCs The Cancer Genome Atlas (TCGA), including for example the pseudo-hypoxic type (germline mutations in *SDHx*, *FH*, and *VHL*, etc.), the kinase-signaling type (germline or somatic mutations in *RET*, *NF1*, *TMEM127*, *MAX*, and *HRAS*, etc.), and the Wnt-signaling type (somatic mutations in *CSDE1* and somatic gene fusions affecting *MAML3*) (Crona *et al*, 2017). However, 50~60% of PCCs fail to be classified using this system (Lenders *et al*, 2014).

As understanding of PCC clinicopathological and immunophenotypic characteristics has deepened, the former concept of 'benign or malignant PCC' has been abandoned; since 2017, all PCCs are regarded as malignant tumors with metastatic potential according to the WHO pathological classification (Lam, 2017; Mete *et al*, 2022). There is no single histo-morphological feature indicating the metastasis risk of PCCs; a number of multifactorial systems have been

proposed (Kulkarni *et al*, 2016). A cytomorphometric study reported that extra-adrenal location, coarse nodularity, confluent necrosis, and the absence of hyaline globules are associated with metastasis risk (Lewis, 1971). Several scoring systems that for example consider vascular invasion, tumor size, diffuse growth, and mitotic activity have been used for risk assessment of metastasis risk of PCCs (Sherwin, 1959; Sisson *et al*, 1984; Symington & Goodall, 1953). A scoring system—the Pheochromocytoma of the Adrenal gland Scaled Score (PASS)—is weighted for histologic features and has been used to separate tumors with a potential for a biologically aggressive behavior (PASS > or = 4) from tumors with benign lesion (PASS < 4) (Thompson, 2002).

Immune checkpoint inhibitors (ICIs) have achieved remarkable results in a variety of solid tumors in recent years (Liu *et al*, 2022; Zhang *et al*, 2020). Currently, there are only 2 clinical trials investigating the efficacy of ICIs for the treatment of metastatic PCCs: one is still in the recruitment stage, and the other showed 43% non-progression rate (NPR) and 0% overall response rate (ORR) in 7 PCC patients (Dai *et al*, 2020; Jimenez *et al*, 2022; Naing *et al*, 2020). The composition of immune cells in the tumor immune microenvironment is an essential indicator for predicting likely responses to immunotherapy, and serves as the basis of immunotherapy (Liu *et al*, 2023; Liu *et al.*, 2022). Despite the application of immunohistochemical staining to characterize the PCC microenvironment (Calsina *et al*, 2023; Tufton *et al*, 2022), limited knowledge exists regarding the cell composition and inter-cellular crosstalk within the PCC microenvironment.

In the present study, we performed single-cell RNA sequencing (scRNA-seq) analysis of 11 tumor tissues and 5 adjacent normal adrenal medullary tissues from 4 sporadic PCC patients with unclassified mutations and 1 hereditary PCC patient with Von Hippel-Lindau (VHL) syndrome caused by germline mutation in *VHL*. We found less intra-tumoral heterogeneity than inter-individual heterogeneity of PCCs. For the unclassified PCCs, we distinguished metabolism-type and kinase-type PCCs based on copy number variants (CNVs) and gene expression profile data. These two PCC types also displayed distinct characteristics of tumor evolution and cell-cell communication. Although multispectral immunofluorescence staining showed a lack of $CD8^+$ T cell infiltration in both metabolism-type and kinase-type PCCs, only the kinase-type PCC exhibited downregulation of *HLA-I* molecules that possibly regulated by *RET*, suggesting the potential of combined therapy with kinase inhibitors and immunotherapy for kinase-type PCCs, whereas the application of immunotherapy to metabolism-type PCCs (with antigen presentation ability) is likely unsuitable. Our study presents a single-cell transcriptomics-based molecular classification and microenvironment characterization of PCCs and provides clues for potential therapeutic strategies to treat PCCs.

RESULTS

A Landscape View of Cell Composition in PCCs

To characterize the molecular correlates of unclassified PCCs based on known prominent driver

alterations, we performed single-cell RNA sequencing (scRNA-seq) on 16 collected specimens from 5 PCC patients (P1-P5). Four of these patients (P1-P4) suffered from sporadic PCCs: whole exome sequencing (WES) of these tumor tissues detected somatic mutations as compared with their adjacent normal adrenal medullary tissues, including in *JAK2*, *ARHGEF39*, *KMT2D*, and *MST1* (Supplemental Table S1); note that none of these fit into the three previously molecularly defined groups in the TCGA molecular taxonomy (Crona *et al.*, 2017). The cohort also included 1 hereditary PCC patient (P5) with Type 2 Von Hippel-Lindau (VHL) syndrome, with a germline missense mutation in *VHL* (Supplemental Table S1).

We collected 1 resected tumor specimen from P1 (P1_T1), 3 specimens from distinct intra-tumoral sites from P2 (P2_T1, P2_T2, and P2_T3) and P5 (P5_T1, P5_T2, and P5_T3), as well as 2 specimens from distinct intra-tumoral sites from P3 (P3_T1 and P3_T2), and P4 (P4_T1 and P4_T2). To enable comparisons, one normal adrenal medullary tissue adjacent to the tumor was collected from each patient (P1_A, P2_A, P3_A, P4_A, and P5_A) (Fig. 1A). The morphology of PCC cells was assessed through hematoxylin-eosin-stained tumor tissues, showing the typical cell arrangement (small alveoli surrounded by fibro-vascular stroma) and characteristic shapes (polygonal or fusiform cells) of PCCs (Lupşan *et al*, 2016) (Supplemental Fig. S1). Meanwhile, immunocytochemistry staining showed robust expression of Chromogranin A (CGA) in these tumor tissues (Supplemental Fig. S1). These pathological evaluations validate the collected samples as PCC tumor specimens (Mete *et al.*, 2022). Additionally, we utilized the PASS scoring system to assess the histological features and evaluate the metastasis risk of PCC patients

(Supplemental Table S2).

The specimens were digested into single cell suspensions, and 3'-scRNA-seq (Chromium Single Cell 3′ v3 Libraries) analysis was performed on each sample. After quality control filtering to remove cells with low gene detection and high mitochondrial gene coverage, we retained 133,894 individual cells (Supplemental Fig. S2A-S2C). SCTansform normalization and principal component analysis (PCA) functions of the Seurat suite (Butler *et al*, 2018; Satija *et al*, 2015; Stuart *et al*, 2019) were then employed for unsupervised dimensionality reduction prior to clustering. Uniform Manifold Approximation and Projection (UMAP) was used for visualizing the distinct specimens, patients, and tissue types (Fig. 1B and 1C).

We classified the 67 detected clusters into 13 cell types according to their expression profiles for recognized marker genes and Spearman correlation analysis between clusters: the classified cell types included adrenal cells (marked by *DLK1* and *RBP1*), endothelial cells (marked by *PECAM1* and *VWF*), fibroblasts (marked by *THY1* and *PLAC9*), smooth muscle cells (marked by *ACTA2* and *TAGLN*), monocytes/macrophages (marked by *CD14* and *CD163*), neutrophils (marked by *S100A8* and *S100A9*), T cells (marked by *IL7R* and *CD3D*), natural killer cells (NKs, marked by *KLRD1* and *GNLY*), proliferating cells (marked by *TOP2A* and *MKI67*), plasma cells (marked by *XBP1* and *IGKC*), B cells (marked by *MS4A1* and *CD79A*), mast cells (marked by *KIT* and *TPSB2*), and sustentacular cells (marked by *S100B* and *CRYAB*) (Fig. 1C and 1D, Supplemental Fig. S2D and S2E). Thus, our clustering and cell type annotation analysis

identified diverse adrenal cells, stromal cells, and immune cells (including lymphocytes and myeloid cells) within the PCC microenvironment (Supplemental Fig. S3).

The Intra-tumoral Heterogeneity was Less Extensive than the Inter-individual Heterogeneity of PCCs

In light of the remarkable diversity of drivers including germline and somatic mutations reported among PCCs (Crona *et al.*, 2017), we investigated PCC heterogeneity at the inter-individual and intra-tumoral levels based on the PASS system and single-cell transcriptional profiles. The PASS scores of 11 collected PCC tissues ranged from 2 to 9, showing obvious heterogeneity among the examined intra-tumoral sites and inter-individual comparisons for the 5 PCC patients (Supplemental Table S2). The Spearman correlation analysis based on average gene expression in each specimen showed that the intra-tumoral heterogeneity was less than inter-individual heterogeneity (Fig. 2A), inconsistent with the PASS score evaluation. We further analyzed the cell type composition in each specimen and found similar fractions of cell types between the collected intra-tumoral sites despite different PASS scores (Fig. 2B), indicating relatively small intra-tumoral differences in both gene expression and cell type composition. These results revealed that scRNA-seq analysis and PASS score represent different levels and dimensions of PCC heterogeneity.

The inter-individual correlation analysis indicated that P4 showed low correlation with the other three sporadic PCCs patients (P1-P3) (Fig. 2C), and further analysis of cell type fractions showed

a significantly elevated proportion of adrenal cells (77%) in P4; the adrenal cells comprised between 16–36% of the total cells in the P1-P3 specimens (Fig. 2D). P4 also had an obviously distinct distribution of stromal cells *vs* immune cells (9% stromal cells and 14% immune cells) as compared to P1-P3 (28-62% stromal cells and 22-43% immune cells) (Fig. 2D). Consistent with the reported vascular endothelial hyperplasia phenotype in VHL syndrome (Vortmeyer *et al*, 2013), it was unsurprising that we observed poor correlation between the sporadic patients (P1-P4) and the VHL patient (P5), reflecting a higher proportion of endothelial cells in P5 (35%) as compared to P1-P4 (3-10%) (Fig. 2C and 2D).

Identification of Tumor Clusters through CNV analysis

To further characterize PCC cells, we collected adrenal cells, which theoretically include adrenocortical cells and chromaffin cells (Yates *et al*, 2013). The copy number karyotyping of aneuploid tumors (CopyKAT) algorithm (Gao *et al*, 2021) was applied, which estimates genomic copy number variants (CNVs) from scRNA-seq data by employing an integrative Bayesian segmentation approach to distinguish PCC cells from normal chromaffin cells. Our analysis identified two clusters among adrenal cells (normal cells and tumor cells), with tumor cells showing extensive chromosomal amplification and/or deletion (Fig. 3A). Consistently, the inferred aneuploid tumor cells highly expressed *Chromogranin B* (*CHGB*), which is a marker of PCC cells (Wiedenmann *et al*, 1988; Winkler & Fischer-Colbrie, 1992) (Fig. 3B and 3C). The inferred diploid normal cells expressing high levels of *CYP17A1* and *HSD3B2* were defined as adrenocortical cells (Kubota-Nakayama *et al*, 2016), while the inferred diploid normal cells

showing low *CHGB* expression were defined as normal chromaffin cells (Fig. 3B and 3C). We also found a cluster of inferred diploid normal cells with high expression of *VWF* (a marker for vascular endothelial cells) in the VHL patient (P5) (Fig. 3B and 3C).

We noticed two CNV patterns among the inferred aneuploid tumor cells, with the distinction evident in chromosomes 3, 11, and 17 (Fig. 3A). These CNV profiles were reflected in distinct tumor clusters (tumor cluster A and B) through CopyKAT prediction (Fig. 3D). We observed that cells in inferred tumor cluster A exhibited high expression of *NDUFA4L2* and *COX4I2*, while cells in inferred tumor cluster B expressed high levels of *PNMT* and *RET* (Fig. 3D and 3E), suggesting the different gene expression between tumor cluster A and B. PNMT is known as an enzyme that catalyzes the conversion of norepinephrine to epinephrine and that RET is a member of the receptor tyrosine kinase family, while NDUFA4L2 and COX4I2 respectively function in the oxidative phosphorylation and glycolysis pathways (Drilon *et al*, 2018; Mahmoodi *et al*, 2020; Sinkler *et al*, 2017). Taken together, we distinguished PCC cells from adrenal cells through CNV analysis and found two clusters of PCC cells with different single-cell copy number profiles.

Definition of Metabolism-type and Kinase-type tumors among unclassified PCCs

To explore the gene expression profile between tumor cluster A and B, we then used the FindAllMarkers function of the Seurat suite (Butler *et al.*, 2018; Satija *et al.*, 2015; Stuart *et al.*, 2019) to identify differentially expressed genes (DEGs) of these tumor clusters (Fig. 4A and 4B). A functional enrichment analysis based on gene ontology (GO) annotation was performed to

further characterize the biological function of tumor clusters: the tumor cluster A DEGs showed functional enrichment for terms including generation of metabolites and energy, response to oxygen levels, response to hypoxia, and ATP metabolic process and some notably upregulated genes of tumor cluster A included known energy metabolism-related genes such as *NDUFA4L2*, *COX4I2*, *RGS4*, and *AQP1* (Fig. 4C). For tumor cluster B, the GO analysis showed enrichment for terms including cytoplasmic translation, neuron projection development, axon development, and cell growth, and there was obvious upregulation of *PNMT*, *RET*, and genes encoding other kinases known to function in proliferation, as well as genes that participate in the regulation of neuroendocrine functions (*e.g.*, *CALM1*, *PENK*, and *NPY*) (Fig. 4D).

Notably, immunocytochemistry staining of serial tumor sections showed strong accumulation of PNMT and RET in P4, while NDUFA4L2 and COX4I2 accumulation was characteristic for the P1-P3 and P5 sections, providing protein-level evidence to validate the differential trends detected from the scRNA-seq results (Fig. 4E). As a consequence, we propose a metabolism-type (P1-P3) and kinase-type (P4) classification for unclassified sporadic PCCs. Consistently, kinase-signaling PCCs by TCGA classification include germline and somatic mutations in *RET*, and are uniquely able to secrete epinephrine, owing to their high expression of *PNMT*; P5 could also be classified into the metabolism-type we defined, which is known to display reprogramming of cellular energy metabolism caused by *VHL* mutation and subsequent *HIF* dysregulation (Chappell *et al*, 2019). When considering clinical information from 5 PCC patients, including tumor size, signs, symptoms and laboratory tests, we observed that P4 exhibited

relatively higher blood pressures and the plasma levels of 3-methoxytyramine and normetanephrine compared to P1-P3, and P5 (Supplemental Table S3), consistent with the high expression of PNMT in the kinase-type PCC patient (Fig. 4E). These results support that the previously unclassified PCCs can be classified as metabolism-type or kinase-type based on transcriptional programs, with these types partially corresponding to the pseudo-hypoxic type and kinase-signaling type of PCCs from the TCGA classification.

Trajectory Analysis Reveals Subclonal Dynamics of PCC Types

We next examined tumor subclonal evolution patterns for the metabolism-type and kinase-type PCCs, by applying the Dynverse algorithm to order cells along a pseudotime trajectory (Saelens *et al*, 2019). We first clustered metabolism-type PCC cells into 2 subclusters based on DEGs and found similar proportions of tumor subcluster 1 and 2 at both the early stage and late stage of tumor evolution (Fig. 5A and 5B). Late up-regulated genes include *S100A4* and *TAGLN* that promote epithelial-mesenchymal transition and cell invasion, which highly expressed in subcluster 2 (Fig. 5C), suggesting the higher metastasis potential of subcluster 2 as compared with subcluster 1. Metabolism-related genes such as *NDUFA4L2*, *ATP5MG*, *NDUFB4*, and *COX17* were highly expressed at early stage, while *SOD3* and *COX7A1* were up-regulated at the late stage (Fig. 5C), revealing the consistently active metabolism phenotype of metabolism-type PCCs cells. We also found the high expression of tumor suppressor gene *SPINT2* at early stage and subsequent up-regulation of the oncogene *JUNB* (Fig. 5C), revealing an increase of metastasis potential over the tumor evolution of metabolism-type PCCs. In short, these results

indicate that cells from metabolism-type PCCs display phenotype of consistently active metabolism and increasingly metastasis potential.

We then clustered kinase-type PCC cells into 2 subclusters and found that the major clone has been changed from subcluster 1 to 2 along the trajectory (Fig. 5D and 5E). Further analysis of DEGs in the pseudotime trajectory showed early high expression of *CALM1* and *CALM2* in the subcluster 1, and late up-regulation of *RET* in the subcluster 2 (Fig. 5F), suggesting the persistent dysregulation of kinase signals over tumor evolution. We also noticed the early expression of *PNMT*, while neuron-specific genes such as *MAP2*, *MAP1B*, *L1CAM*, and *CNTN1* were up-regulated later in the pseudotime trajectory (Fig. 5F), suggesting the decrease of epinephrine synthesis and the appearance of neuron-like phenotypes during tumor evolution, consistent with previously reported neuron-like phenotypes in PCC cells with high expression of RET (Califano *et al*, 1995; Powers *et al*, 2003; Powers *et al*, 2009). Taken together, these analyses have revealed the transcriptional clonal dynamics of metabolic-type and kinase-type PCCs.

Cell-cell Communication Analysis to Further Characterize the Tumor Microenvironment

Having characterized differences in the cell type composition, gene expression, and clonal evolution between metabolism-type and kinase-type PCCs, we subsequently expanded our investigation to cell-cell communication occurring within the distinct tumor microenvironments of these two types of PCCs. We adopted CellChat tool to quantitively analyze inter-cellular communication networks (Jin *et al*, 2021). We observed the activation of the annexin signaling

pathway in metabolism-type PCCs (Fig. 6A). Further analysis of participated ligand-receptors showed major participation of *ANXA1-FPR1* pair in the annexin signaling pathway (Fig. 6B), and high co-expression of *ANXA1* and *FPR1* in neutrophils and monocytes/macrophages (Fig. 6C). It has been reported that the annexin signaling pathway is known to be activated under a strong inflammatory reaction (Gastardelo *et al*, 2014; Gavins *et al*, 2003; Gerke & Moss, 2002; Hayhoe *et al*, 2006). Combined with our findings of a higher proportion of neutrophils and monocytes/macrophages in metabolism-type as compared with kinase-type (Supplemental Fig. S4), we speculate that metabolism-type PCCs may display elevated inflammatory responses. We then performed Gene Set Enrichment Analysis (GSEA) on metabolism-type and kinase-type PCCs by using hallmark gene sets in the MSigDB databases (Liberzon *et al*, 2011). As expected, the inflammatory response signaling pathway showed enrichment in metabolism-type PCCs as compared with that in kinase-type PCC (Fig. 6D). Taken together, metabolism-type PCCs exhibited a strong inflammatory reaction and the activation of annexin signaling pathway.

Considering the heterogeneity in cell type composition between sporadic and VHL patients in metabolism-type, we further analyzed inter-cellular interactions in the VHL patient. We noticed the activation of VEGF signaling pathway in P5 (Fig. 6E), and major contribution of *PLGF-VEGFR1*, *VEGFA-VEGFR1* and *VEGFA-VEGFR2* pairs to VEGF signaling pathway (Fig. 6F). Specifically, *VEGFA* and *VEGFR1* were highly expressed in tumor cells, *VEGFR1* and *VEGFR2* in endothelial cells, and *PLGF* in fibroblasts and smooth muscle cells, respectively (Fig. 6G), suggesting the crosstalk between tumor cells and fibroblasts or endothelial cells in tumor

microenvironment through these ligand-receptor pairs, which mediated in the tumor angiogenesis and metastasis. The observed activation of VEGF pathway is consistent with the vascular endothelial hyperplasia caused by *VHL* mutation in VHL syndrome (Vortmeyer *et al.*, 2013) and the elevated proportion of endothelial cells in this patient (Fig. 2D).

We subsequently analyzed the kinase-type PCC patient, and identified the activation of FGF signaling network (Fig. 6H) and major involvement of *FGF1-FGFR1* in the FGF pathway (Fig. 6I). The smooth muscle cells, fibroblasts, and B cells exhibited high expression of *FGF1*, while tumor cells, smooth muscle cells, T cells, and B cells highly expressed *FGFR1* (Fig. 6J). The analyses suggested the cell-cell communication among tumor cells, stroma cells, and immune cells through the *FGF1-FGFR1* pair, which regulated the tumor cell proliferation (Katoh, 2016). These results indicate that kinase-type PCCs may benefit from FGFR inhibitors, which have been shown to exert inhibitory effects on tumor proliferation (Liang *et al*, 2012). Together, we described the inter-cellular communication networks in microenvironment of metabolism-type and kinase-type PCCs.

Immune Infiltration in the PCC Microenvironment Implies Patient Responses to Immunotherapy

We further analyzed the immune microenvironment of metabolism-type and kinase-type PCCs. Visualization of inter-cellular communication showed apparent crosstalk between tumor cells

and T cells in metabolism-type patients, while we were surprised to find a lack of apparent communication between tumor cells and T cells in the kinase-type patient (Fig. 7A). These results suggested that kinase-type PCC cells could evade immune surveillance of T cells and further indicated the immune escape potential of kinase-type PCCs. Considering leukocyte antigen-class I (HLA-I) surface level is known to represent the antigen-presenting abilities of tumor cells (Brea *et al*, 2016; Jhunjhunwala *et al*, 2021; Oh *et al*, 2019), we assessed *HLA-I* expression in PCC cells: the expression levels of *HLA-A*, *HLA-B*, and *HLA-C* were significantly lower in kinase-type PCC cells than in metabolism-type PCC cells (Fig. 7B). Consistently, immunohistochemistry staining of serial sections of tumor tissues showed lower expression of HLA-A in P4 as compared to that in other patients (Fig. 7C), providing a plausible explanation for the lack of interactions detected between tumor cells and T cells in the kinase-type PCC. In short, we discovered that the kinase-type PCC displayed an impaired *HLA-I* expression profile consistent with immune escape, while metabolism-type PCCs showed antigen-presenting abilities.

We additionally assessed the immune microenvironment of PCCs by subclustering immunotherapy-related immune cells and identified 8 clusters including central memory $CD4^+$ T cells ($CD4^+$ TCM, marked by *CD3D*, *CD3E*, *CD3G*, *CD4*, *CCR7*, and *IL7R*), effector memory $CD4^+$ T cells ($CD4^+$ TEM, marked by *CD3D*, *CD3E*, *CD3G*, *CD4*, and *IL7R*), $CD8^+$ T cells (marked by *CD3D*, *CD3E*, *CD3G*, *CD8A* and *CD8B*), natural killer T cells (NKTs, marked by *CD3E*, *KLRD1* and *GNLY*), natural killer cells (NKs, marked by *KLRD1* and *GNLY*), B cells

(marked by *MS4A1* and *CD79A*), M1 macrophages (marked by *CD68*), and M2 macrophages (marked by *CD68* and *CD163*) (Fig. 7D and 7E). Further analysis of immune cell type composition in metabolism-type and kinase-type PCCs showed an increase in the proportion of $CD4^+$ T cells, $CD8^+$ T cells, and M1 macrophages in tumor tissues as compared with that in adjacent normal adrenal medullary tissues, while the proportion of M2 macrophages in adjacent normal adrenal medullary tissues decreased as compared with that in tumor tissues (Fig. 7F).

The proportion and location of infiltrating immune cells in tumor tissues have been shown to be informative regarding responsivity to immunotherapy (Sade-Feldman *et al*, 2018; Stanton & Disis, 2016). In particular, the $CD8^+$ T cells play an essential role in anti-tumor immunity; these cells can recognize tumor antigens displayed on the surface of tumor cells by HLA-I molecules (Jhunjhunwala *et al.*, 2021). As the scRNA-seq data do not support discernment of whether immune cells have infiltrated tumors or are merely present in the sampled materials, we performed multispectral immunofluorescence (mIF) staining on $CD4^+$ T cells, $CD8^+$ T cells, M1 macrophages, and M2 macrophages in formalin-fixed paraffin-embedded (FFPE) tumor tissues of P1-P5. We observed that $CD8^+$ T cells, as well as $CD4^+$ T cells, M1 macrophages, and M2 macrophages were rare (and were only present in tumor stroma of P1-P5), indicating apparent immune escape in both metabolism-type and kinase-type PCCs (Fig. 7G). Combined with previously reported negative regulatory effects of kinases (such as RET, ALK, and MEK) on HLA-I expression on tumor cells (Brea *et al.*, 2016; Oh *et al.*, 2019), we speculate that the possible reason for inability in recruiting $CD8^+$ T cells of kinase-type PCCs is the down-

regulation of *HLA-I* in tumor cells regulated by *RET*, while the mechanism of immune escape in metabolism-type PCCs (with antigen presentation ability) needs to be further explored. Our results also indicate that the application of immunotherapy to metabolism-type PCCs is likely unsuitable, while kinase-type PCCs may have the potential of combined therapy with kinase inhibitors and immunotherapy.

DISCUSSION

The genomic research of PCCs has made continuous progress in recent years (Bausch *et al*, 2017; Mete *et al.*, 2022; Neumann *et al*, 2019; Nölting *et al.*, 2022), but there have been obvious breakthroughs for more efficacious therapies. Isotope therapies can only relieve the clinical symptoms in 50% of patients (without reducing tumor size) (Fitzgerald *et al*, 2006; Roman-Gonzalez & Jimenez, 2017), while most chemotherapies and targeted therapies exhibit low remission rates and severe side effects in clinical studies (Druce *et al*, 2009; Hamidi, 2019; O'Kane *et al*, 2019; Oh *et al*, 2012), limiting the development of PCC treatments. Although immunotherapy has achieved success in the therapy of solid tumors, it is difficult to evaluate the curative effect in PCCs. To address this problem, two key features associated with the tumor immunotherapy need to be elucidated—tumor heterogeneity and the tumor microenvironment (Hegde & Chen, 2020; Li *et al*, 2018; Liu *et al.*, 2023; Liu *et al.*, 2022; Zhang & Zhang, 2020). Regarding PCC heterogeneity, genomic studies have confirmed the inter-individual heterogeneity based on driver mutations (Dahia, 2014; Jhawar *et al*, 2022; Sarkadi *et al*, 2022;

Toledo *et al.*, 2017). However, there is lack of relevant research on intra-tumoral heterogeneity, which has an impact on disease progression and sensitivity to immunotherapy (Vitale *et al*, 2021). For the PCC microenvironment, the cell composition and inter-cellular crosstalk remain largely unexplored. By investigating the heterogeneity and microenvironment characteristics of PCCs, we proposed a feasible method to judge the heterogeneity of PCCs, and also provided a clue for the application of immunotherapy in PCC patients.

The clinical and histopathological diagnosis of metastasis risk and heterogeneity of PCCs is particularly difficult, and is still limited by the lack of reliable prognostic markers (de Wailly *et al*, 2012). Although the PASS scoring system was proposed as a tool for discriminating potentially metastasis PCCs from benign ones, its utility is somewhat restricted due to observer variation and nonrepeatability (Agarwal *et al*, 2010; Kimura *et al*, 2014; Thompson, 2002; Wu *et al*, 2009). By integrating the PASS scoring system with scRNA-seq analysis, we observed that both methods offered complementary insights into the intra-tumoral and inter-individual heterogeneity of PCCs. Considering the intricate cellular components within the PCC microenvironment and recognizing the advantage of scRNA-seq in dissecting the tumor microenvironment (Ren *et al*, 2021), the potential integration of molecular diagnostic methods, such as single-cell sequencing, with pathological tools appears promising for implementation in the clinical practice of PCC diagnosis and care (Crona *et al.*, 2017; Papathomas *et al*, 2021).

According to the results of genomics research in recent years, 40~50% of PCCs have been classified into a certain molecular pathway (pseudohypoxia, kinase, or Wnt), but the remaining 50-60% are still unclassified (Crona *et al.*, 2017; Lenders *et al.*, 2014). PCCs that classified into these molecular pathways may have the opportunity to carry out drug clinical trials against corresponding targets, such as HIF2α, VEGF, and RET, etc. (Jhawar *et al.*, 2022; Nölting *et al*, 2019; Toledo & Jimenez, 2018), while unclassified PCCs still have no clues or basis for drug treatment. According to the WES results of the 5 patients in our study, except for one patient with *VHL* germline mutation, the others could not be classified based on detected germline or somatic mutations. Therefore, we developed a new classification of PCCs based on scRNA-seq, which are able to accurately capture the transcriptional features of PCC cells. We found that PCC cells from 4 patients highly expressed metabolism-related genes, while that from another patient exhibited high expression of kinase-related genes. Although previous studies applying bulk RNA-seq analysis of PCCs have also reported highly expressed genes (Batchu *et al*, 2022; Flynn *et al*, 2015), the interpretation of bulk RNA-seq data can be complicated by interference from the large number of non-tumor cells (Huang *et al*, 2023; Li *et al*, 2022), so it is difficult to determine whether the highly expressed genes are reliable molecular features of PCCs. Our study revealed that the kinase-type PCC patient (P4) exhibited higher blood pressures and plasma levels of catecholamine metabolites (3-methoxytyramine and normetanephrine). Further research is warranted to explore the correlation of our molecular classification with plasma levels of catecholamine metabolites.

The tumor immune microenvironment, defined as the interplay between tumor cell antigen presentation, immune cell infiltration, and their interactions, can be multifaceted (de Visser & Joyce, 2023; Hanahan, 2022). Given the spatial limitations of scRNA-seq and the protein detection constraints of multispectral immunofluorescent staining, we combined these two methods to investigate immune escape mechanisms in both types of PCCs. Although our immunofluorescence staining data showed a lack of $CD8^+$ T cell infiltration in both metabolism-type and kinase-type PCCs, only kinase-type PCCs exhibited downregulation of *HLA-I* molecules. The expression of HLA-I is a marker for tumor antigen presentation and $CD8^+$ T cell infiltration (Jhunjhunwala *et al.*, 2021; Perea *et al*, 2018; Sadagopan *et al*, 2022). Previous studies have demonstrated that kinases such as RET, MAP2K1, ALK, and FGF can promote tumor growth via helping tumor cells to evade the immune system by downregulating HLA-I expression (Brea *et al.*, 2016; Oh *et al.*, 2019). The kinase-type PCCs that we defined exhibited activation of RET and FGF signals, which led us to consider the possible inhibitory effect of kinases on HLA-I expression in PCCs. Recently, RET inhibitors have been approved for the treatment of non-small cell lung cancer with *RET* mutation (Drilon *et al*, 2020; Griesinger *et al*, 2022). For kinase-type PCCs, whether RET inhibitors can enhance the antigen presentation ability of tumor cells, and further provide chance for combination of kinase-targeted therapy and immunotherapy, needs to be verified by follow-up research. The metabolism-type PCCs, however, with antigen presentation ability and also the lack of $CD8^+$ T cell infiltration, the application of immunotherapy is likely unsuitable, and the mechanism(s) of immune escape in these tumors needs to be further explored.

There are potential limitations of our study. Despite the patient cohort in our study including a hereditary PCC patient, only one patient with a *VHL* germline mutation was included; other types of hereditary PCCs with germline mutations (for example in *SDHx* and *FH*) were not included. The number of sporadic cases was also limited, mainly caused by the low incidence of PCCs. In addition, the specimens were all from primary tumors, while no metastatic tumors were included. Together, these considerations underscore the necessary for additional studies of PCCs in the future.

In summary, our study presents the molecular classification and tumor microenvironment characterization of PCCs through scRNA-seq. The intra-tumoral heterogeneity is lower than the inter-individual heterogeneity of PCCs. Among unclassified PCCs, we defined metabolism-type and kinase-type at the single-cell transcriptome level. We observed a lack of $CD8^+$ T cell infiltration in both metabolism-type and kinase-type PCCs. The kinase-type PCC showed downregulation of *HLA-I* that possibly regulated by *RET*, suggesting the potential of combined therapy with kinase inhibitors and immunotherapy in kinase-type PCCs. For the metabolism-type PCCs, which have antigen presentation ability and also exhibit immune escape, the application of immunotherapy is likely unsuitable. The proposal of this molecular classification and our characterization of these PCC types can contribute to strategy development and clinical trials of PCC treatments in the future.

METHODS

Ethical Regulations

The research presented here complies with all relevant local, national, and international regulations. For all PCC patient specimens, informed written consent was obtained prior to donation. The Peking University First Hospital Review Board (Protocol 300-001) approved the study.

Patient Cohort

Five PCC patients were included, and all patients had signed the consent forms at the Department of Urology in Peking University First Hospital. Fresh tumor specimens were collected during surgical resection. The sporadic patients (P1-P4) were performed surgical resections of the tumors at right adrenals, and the VHL patient (P5) underwent left adrenalectomy. We collected 1 resected tumor specimen from P1 (P1_T1), 3 specimens from distinct intra-tumoral sites from P2 (P2_T1, P2_T2, and P2_T3) or P5 (P5_T1, P5_T2, and P5_T3), and 2 specimens from distinct intra-tumoral sites from P3 (P3_T1 and P3_T2), or P4 (P4_T1 and P4_T2). To enable comparisons, one normal adrenal medullary tissue adjacent to the tumor was collected from each patient (P1_A, P2_A, P3_A, P4_A, and P5_A). A total of sixteen specimens were carefully dissected under the microscope and confirmed by a qualified pathologist.

Tissue Processing

The fresh tumor specimens were stored in the tissue preservation solution (JSENB) and washed with Hanks Balanced Salt Solution (HBSS, HyClone) for 3 times and minced into 1-2 mm pieces. Then the tissue pieces were digested with 2 ml tissue dissociation solution at 37°C for 15 min in 15 ml centrifuge tube with sustained agitation. After digestion, using 40 μm sterile strainers to filter the samples and centrifuging the samples at 1,000 rpm for 5 min. Then the supernatant was discarded, and the sediment was resuspended in 1 ml phosphate buffered saline (PBS, Solarbio). To remove the red blood cells, 2 ml red blood cell lysis buffer (BD) was added at 25°C for 10 min. The solution was then centrifuged at 500 g for 5 min and suspended in PBS. The cells were stained with trypan blue (Sigma) and microscopically evaluated.

Single-cell Library Construction and Sequencing

Utilizing the 10x Genomics Chromium Single Cell 3′ v3 Library Kit and Chromium instrument, approximately 17,500 cells were partitioned into nanoliter droplets to achieve single-cell resolution for a maximum of 10,000 individual cells per sample. The resulting cDNA was tagged with a common 16 nt cell barcode and 10 nt Unique Molecular Identifier during the RT reaction. Full-length cDNA from poly-A mRNA transcripts was enzymatically fragmented and size selected to optimize the cDNA amplicon size (approximately 400 bp) for library construction (10x Genomics). The concentration of the 10x single-cell library was accurately determined through qPCR (Kapa Biosystems) to produce cluster counts appropriate for the HiSeq4000 or NovaSeq6000 platform (Illumina). In all, 26 × 98 bp (3′ v3 libraries) sequence data were

generated targeting between 25 and 50K read pairs/cell, which provided digital gene expression profiles for each individual cell.

General scRNA-seq Data Analysis

For single-cell RNA-seq analysis, we used CellRanger (10x Genomics, v.6.1.2) to pre-process the single-cell RNA-seq data after obtaining the paired-end raw reads. Cell barcodes and unique molecular identifiers (UMIs) of the library were extracted from read 1. Then, the reads were split according to their cell (barcode) IDs, and the UMI sequences from read 2 were simultaneously recorded for each cell. Quality control on these raw readings was subsequently performed to eliminate adapter contamination, duplicates, and low-quality bases. After filtering barcodes and low-quality readings that were not related to cells, we mapped the cleaned readings to the human genome (GRCh38) and retained the uniquely mapped readings for UMIs counts. Next, we estimated the accurate molecular counts and generated a UMI count matrix for each cell by counting UMIs for each sample. Finally, we generated a gene-barcode matrix that showed the barcoded cells and gene expression counts.

The R package Seurat (v.4.0.2) was used for all subsequent analysis (Butler *et al.*, 2018; Satija *et al.*, 2015; Stuart *et al.*, 2019). For quality control of single-cell RNA-seq, a series of quality filters was applied to the data to remove those barcodes which fell into any one of these categories: too few genes expressed (possible debris), too many UMIs associated (possible more than one cell), and too high mitochondrial gene expression (possible dead cell). The cutoffs for

these filters were as follows: the minimum number (no less than 200) and maximum number (no more than 5000) were used in controlling the number of genes; the maximum number (no more than 30%) was used for the quality control of the percentage of mitochondrial genes. Low-quality cells and outliers were discarded, and the single cells that passed the QC criteria were used for downstream analyses.

Cell Clustering and Cell Type Annotation

The Seurat software package (v.4.0.2) was used to perform cell clustering analysis to identify major cell types (Butler *et al.*, 2018; Satija *et al.*, 2015; Stuart *et al.*, 2019). All Seurat objects constructed from the filtered UMI-based gene expression matrixes of given samples were merged. We first applied the SCTransform (v.0.3.2) function to implement normalization, variance stabilization, and feature selection through a regularized negative binomial model. Then, the principal component analysis (PCA) was applied for linear dimensionality reduction with the top 3000 variable genes. According to standard steps implemented in Seurat, highly variable numbers of principal components (PCs) 1-50 were selected and used for clustering using the Uniform Manifold Approximation and Projection (UMAP) method. We identified cell types of these clusters based on the expression of canonic cell type markers or inferred by CellMarker database (Zhang *et al*, 2019). The cluster markers were also certified using the FindAllMarkers function of the Seurat suite, and cell types were manually annotated based on certified markers finally.

Correlation Analysis of scRNA-seq

After integration, for each cluster, each sample, and each patient, we compared the gene expression to others to identify the significant highly expressed genes (adjusted P-value < 0.05 and log fold change > 0). Then the average gene expressions in each cluster, each sample, and each patient were calculated. The pairwise correlations were then estimated.

DEGs Identification and Enrichment Analysis

The cluster-specific genes were identified by running Seurat containing the function of FindAllMarkers on a log-transformed expression matrix (min. pct = 0. 25, only. Pos = TRUE, and logfc.threshold = 0.25). We also identified the differentially over-expressed genes between two clusters with the Wilcoxon Rank-Sum Test with the FindMarkers function in Seurat (adjusted P-value < 0.05, only.pos = T, and logfc.threshold = 0.1), and the cluster-specific overrepresented GO biological process was calculated with the compareCluster function in the clusterProfiler package (v.4.2.2) of R (Yu *et al*, 2012). We also used the GSEA with the curated gene sets to identify the pathways that were induced or repressed in between the cell clusters. In brief, the mean gene expression level was calculated and the log twofold change (FC) between the specific cell cluster and the other cells was applied as the test statistic. The 50-hallmark gene sets in the MSigDB databases (https://www.gsea-msigdb.org/gsea/msigdb) were used for the GSEA analysis (Liberzon *et al.*, 2011).

Single-cell RNA CNV Detection and Clustering

All cells were classified as either normal or tumor based on the genome-wide copy number profiles computed from the gene expression UMI matrix using the Bayesian segmentation approach, CopyKat (v.1.0.8) (Gao *et al.*, 2021). Aneuploid single cells with genome-wide copy number aberrations were anticipated to be tumor cells, while diploid cells were presumed to be normal cells. The CopyKat-based predictions were subsequently validated by single-cell gene expression profiles.

Trajectory Analysis of scRNA-Seq Data

In order to perform a detailed comparison among different trajectory modeling tools, the Dynverse (v.0.1.2) tool was used (Saelens *et al.*, 2019). Based on the scoring system provided by Dynverse and following a careful inspection of the generated trajectories, we applied 'SCORPIUS' and 'EMBEDDR' to infer the development trajectories. Finally, we selected the genes that were differentially expressed on different stages through the trajectory and plotted the pseudotime heatmap.

Cell-cell Communication Analysis

Cell-cell interactions based on the expression of known ligand-receptor pairs in different cell types were inferred using CellChatDB (v.1.1.3) (Jin *et al.*, 2021). In brief, we followed the official workflow and loaded the normalized counts into CellChat and applied the preprocessing functions 'identifyOverExpressedGenes', 'identifyOverExpressedInteractions', and

‘projectData’ with standard parameters set. As database we selected the ‘Secreted Signaling’ pathways and used the pre-compiled human ‘Protein-Protein-Interactions’ as a priori network information. For the main analyses the core functions ‘computeCommunProb’, ‘computeCommunProbPathway’, and ‘aggregateNet’ were applied using standard parameters and fixed randomization seeds. Finally, to determine the senders and receivers in the network, the function ‘netAnalysis_signalingRole’ was applied on the ‘netP’ data slot.

Whole Exome Sequencing and Analysis

Genomic DNA extracted from tumor tissues were sent for whole exome sequencing. The exomes were captured using the Agilent SureSelect Human All Exon V6 Kit and the enriched exome libraries were constructed and sequenced on the Illumina NovaSeq 6000 platform to generate WES data (150 bp paired-end reads, > 100×) according to standard manufacturer protocols. The cleaned reads were aligned to the human reference genome sequence UCSC Build 19 (hg19) using Burrows-Wheeler Aligner (BWA) (v.0.7.12) (Li & Durbin, 2009). All aligned BAM were then performed through the same bioinformatics pipeline according to GATK Best Practices (v.3.8) (McKenna *et al*, 2010). We obtained germline variants based on variant calling from GATK-HaplotypeCaller. We then used GATK-MuT ect2 to call somatic variants in tumors and obtained a high-confidence mutation set after rigorous filtering by GATK-FilterMutectCalls. All variants were annotated using ANNOVAR (v.2018Apr16) (Wang *et al*, 2010).

Immunocytochemistry and Multispectral Immunofluorescent Staining

Immunocytochemistry and multispectral immunofluorescent staining experiments were conducted according to standard protocols using antibodies against formalin-fixed paraffin-embedded (FFPE) tissue specimens. The antibodies used are listed as follows: CGA (ABclonal, A9576), NDUFA4L2 (Proteintech, 66050-1-lg), COX4I2 (Santa, sc-100522), PNMT (Abcam, ab154282), RET (Abcam, ab134100), CD4 (Abcam, ab133616), CD8 (Invitrogen, MA1-80231), CD68 (Invitrogen, MA5-12407), CD163 (Abcam, ab182422), and HLA-A (ABclonal, A11406).

DATA AVAILABILITY

Fastq raw data and processed data can be requested by contacting the corresponding authors. Human transcriptome reference used for our analysis is available at 10x Genomics website (https://cf.10xgenomics.com/supp/cell-exp/refdata-cellranger-GRCh38-3.0.0.tar.gz) or in zenodo (https://zenodo.org/record/4114854/files/refdata-cellranger-GRCh38-3.0.0.tar.gz?download=1).

CODE AVAILABILITY

The single-cell RNA sequencing data was processed using cellranger v.6.1.2 (https://www.10xgenomics.com/) and analyzed with the R package Seurat v.4.0.2 (https://satijalab.org/seurat/). Custom code that was created for scRNA-seq analysis can be requested by contacting the corresponding authors.

ACKNOWLEDGMENTS

This work was supported by grant from Ministry of Science and Technology of China (No. 2021YFA1300603 to L.S.), grant (Z200020 to L.S.) from the Natural Science Foundation of Beijing, grant (82188102 and 31991164 to Y. S., 81874158 and 32370620 to L.S.) from the National Natural Science Foundation of China, and grant (2022CX08 to Z.Z.) from National High-Level Hospital Clinical Research Funding. We thank the National Center for Protein Sciences at Peking University (Beijing, China) and Dr. Jiaqian Wang (YuCe Biotech Co., Ltd) for providing technical support.

AUTHOR CONTRIBUTIONS

Z.Z., L.S., and K.G. conceived the idea and designed the study. Y.X. prepared samples for scRNA-seq. S.Q. performed scRNA-seq data analysis. Q.S., S.F., W.A., Y.X., and W.H. performed immunocytochemistry and multispectral immunofluorescent staining. S.Y., K.Z., and X.Z. provided technical assistance. Z.Z., L.S., and Y.W. provided guidance in data analysis and interpretation of the results. S.Q. drafted the manuscript, with significant input from Z.Z., L.S., and K.G. All authors reviewed the manuscript prior to submission.

CONFLICT of INTEREST STATEMENTS

The authors declare no conflicts of interest that pertain to this work.

REFERENCES

Agarwal A, Mehrotra PK, Jain M, Gupta SK, Mishra A, Chand G, Agarwal G, Verma AK, Mishra SK, Singh U (2010) Size of the tumor and pheochromocytoma of the adrenal gland scaled score (PASS): can they predict malignancy? *World J Surg* 34: 3022-3028

Batchu S, Hakim A, Henry OS, Madzo J, Atabek U, Spitz FR, Hong YK (2022) Transcriptome-guided resolution of tumor microenvironment interactions in pheochromocytoma and paraganglioma subtypes. *Journal of endocrinological investigation* 45: 989-998

Bausch B, Schiavi F, Ni Y, Welander J, Patocs A, Ngeow J, Wellner U, Malinoc A, Taschin E, Barbon G *et al* (2017) Clinical Characterization of the Pheochromocytoma and Paraganglioma Susceptibility Genes SDHA, TMEM127, MAX, and SDHAF2 for Gene-Informed Prevention. *JAMA oncology* 3: 1204-1212

Brea EJ, Oh CY, Manchado E, Budhu S, Gejman RS, Mo G, Mondello P, Han JE, Jarvis CA, Ulmert D *et al* (2016) Kinase Regulation of Human MHC Class I Molecule Expression on Cancer Cells. *Cancer Immunol Res* 4: 936-947

Butler A, Hoffman P, Smibert P, Papalexi E, Satija R (2018) Integrating single-cell transcriptomic data across different conditions, technologies, and species. *Nat Biotechnol* 36: 411-420

Califano D, Monaco C, de Vita G, D'Alessio A, Dathan NA, Possenti R, Vecchio G, Fusco A, Santoro M, de Franciscis V (1995) Activated RET/PTC oncogene elicits immediate early and delayed response genes in PC12 cells. *Oncogene* 11: 107-112

Calsina B, Piñeiro-Yáñez E, Martínez-Montes Á M, Caleiras E, Fernández-Sanromán Á, Monteagudo M, Torres-Pérez R, Fustero-Torre C, Pulgarín-Alfaro M, Gil E *et al* (2023) Genomic and immune landscape Of metastatic pheochromocytoma and paraganglioma. *Nature communications* 14: 1122

Chappell JC, Payne LB, Rathmell WK (2019) Hypoxia, angiogenesis, and metabolism in the hereditary kidney cancers. *J Clin Invest* 129: 442-451

Crona J, Taïeb D, Pacak K (2017) New Perspectives on Pheochromocytoma and Paraganglioma: Toward a Molecular Classification. *Endocrine reviews* 38: 489-515

Dahia PL (2014) Pheochromocytoma and paraganglioma pathogenesis: learning from genetic heterogeneity. *Nature reviews Cancer* 14: 108-119

Dai C, Liang S, Sun B, Kang J (2020) The Progress of Immunotherapy in Refractory Pituitary Adenomas and Pituitary Carcinomas. *Front Endocrinol (Lausanne)* 11: 608422

de Visser KE, Joyce JA (2023) The evolving tumor microenvironment: From cancer initiation to metastatic outgrowth. *Cancer cell* 41: 374-403

de Wailly P, Oragano L, Radé F, Beaulieu A, Arnault V, Levillain P, Kraimps JL (2012) Malignant pheochromocytoma: new malignancy criteria. *Langenbecks Arch Surg* 397: 239-246

Drilon A, Hu ZI, Lai GGY, Tan DSW (2018) Targeting RET-driven cancers: lessons from evolving preclinical and clinical landscapes. *Nature reviews Clinical oncology* 15: 151-167

Drilon A, Oxnard GR, Tan DSW, Loong HHF, Johnson M, Gainor J, McCoach CE, Gautschi O, Besse B, Cho BC *et al* (2020) Efficacy of Selpercatinib in RET Fusion-Positive Non-Small-Cell Lung Cancer. *The New England journal of medicine* 383: 813-824

Druce MR, Kaltsas GA, Fraenkel M, Gross DJ, Grossman AB (2009) Novel and evolving therapies in the treatment of malignant phaeochromocytoma: experience with the mTOR inhibitor everolimus (RAD001). *Hormone and metabolic research = Hormon- und Stoffwechselforschung = Hormones et metabolisme* 41: 697-702

Favier J, Amar L, Gimenez-Roqueplo AP (2015) Paraganglioma and phaeochromocytoma: from genetics to personalized medicine. *Nature reviews Endocrinology* 11: 101-111

Fishbein L, Leshchiner I, Walter V, Danilova L, Robertson AG, Johnson AR, Lichtenberg TM, Murray BA, Ghayee HK, Else T *et al* (2017) Comprehensive Molecular Characterization of Pheochromocytoma and Paraganglioma. *Cancer cell* 31: 181-193

Fitzgerald PA, Goldsby RE, Huberty JP, Price DC, Hawkins RA, Veatch JJ, Dela Cruz F, Jahan TM, Linker CA, Damon L *et al* (2006) Malignant pheochromocytomas and paragangliomas: a phase II study of therapy with high-dose 131I-metaiodobenzylguanidine (131I-MIBG). *Annals*

of the New York Academy of Sciences 1073: 465-490

Flynn A, Benn D, Clifton-Bligh R, Robinson B, Trainer AH, James P, Hogg A, Waldeck K, George J, Li J *et al* (2015) The genomic landscape of phaeochromocytoma. *The Journal of pathology* 236: 78-89

Gao R, Bai S, Henderson YC, Lin Y, Schalck A, Yan Y, Kumar T, Hu M, Sei E, Davis A *et al* (2021) Delineating copy number and clonal substructure in human tumors from single-cell transcriptomes. *Nat Biotechnol* 39: 599-608

Gastardelo TS, Cunha BR, Raposo LS, Maniglia JV, Cury PM, Lisoni FC, Tajara EH, Oliani SM (2014) Inflammation and cancer: role of annexin A1 and FPR2/ALX in proliferation and metastasis in human laryngeal squamous cell carcinoma. *PLoS One* 9: e111317

Gavins FN, Yona S, Kamal AM, Flower RJ, Perretti M (2003) Leukocyte antiadhesive actions of annexin 1: ALXR- and FPR-related anti-inflammatory mechanisms. *Blood* 101: 4140-4147

Gerke V, Moss SE (2002) Annexins: from structure to function. *Physiol Rev* 82: 331-371

Griesinger F, Curigliano G, Thomas M, Subbiah V, Baik CS, Tan DSW, Lee DH, Misch D, Garralda E, Kim DW *et al* (2022) Safety and efficacy of pralsetinib in RET fusion-positive non-small-cell lung cancer including as first-line therapy: update from the ARROW trial. *Annals of oncology : official journal of the European Society for Medical Oncology* 33: 1168-1178

Hamidi O (2019) Metastatic pheochromocytoma and paraganglioma: recent advances in prognosis and management. *Current opinion in endocrinology, diabetes, and obesity* 26: 146-154

Hanahan D (2022) Hallmarks of Cancer: New Dimensions. *Cancer discovery* 12: 31-46

Hayhoe RP, Kamal AM, Solito E, Flower RJ, Cooper D, Perretti M (2006) Annexin 1 and its bioactive peptide inhibit neutrophil-endothelium interactions under flow: indication of distinct receptor involvement. *Blood* 107: 2123-2130

Hegde PS, Chen DS (2020) Top 10 Challenges in Cancer Immunotherapy. *Immunity* 52: 17-35

Huang D, Ma N, Li X, Gou Y, Duan Y, Liu B, Xia J, Zhao X, Wang X, Li Q *et al* (2023) Advances in single-cell RNA sequencing and its applications in cancer research. *Journal of hematology &*

oncology 16: 98

Jhawar S, Arakawa Y, Kumar S, Varghese D, Kim YS, Roper N, Elloumi F, Pommier Y, Pacak K, Del Rivero J (2022) New Insights on the Genetics of Pheochromocytoma and Paraganglioma and Its Clinical Implications. *Cancers* 14

Jhunjhunwala S, Hammer C, Delamarre L (2021) Antigen presentation in cancer: insights into tumour immunogenicity and immune evasion. *Nature reviews Cancer* 21: 298-312

Jimenez C, Armaiz-Pena G, Dahia PLM, Lu Y, Toledo RA, Varghese J, Habra MA (2022) Endocrine and Neuroendocrine Tumors Special Issue-Checkpoint Inhibitors for Adrenocortical Carcinoma and Metastatic Pheochromocytoma and Paraganglioma: Do They Work? *Cancers* 14

Jin S, Guerrero-Juarez CF, Zhang L, Chang I, Ramos R, Kuan CH, Myung P, Plikus MV, Nie Q (2021) Inference and analysis of cell-cell communication using CellChat. *Nature communications* 12: 1088

Katoh M (2016) Therapeutics Targeting FGF Signaling Network in Human Diseases. *Trends in pharmacological sciences* 37: 1081-1096

Kimura N, Takayanagi R, Takizawa N, Itagaki E, Katabami T, Kakoi N, Rakugi H, Ikeda Y, Tanabe A, Nigawara T *et al* (2014) Pathological grading for predicting metastasis in phaeochromocytoma and paraganglioma. *Endocrine-related cancer* 21: 405-414

Kubota-Nakayama F, Nakamura Y, Konosu-Fukaya S, Azmahani A, Ise K, Yamazaki Y, Kitawaki Y, Felizola SJ, Ono Y, Omata K *et al* (2016) Expression of steroidogenic enzymes and their transcription factors in cortisol-producing adrenocortical adenomas: immunohistochemical analysis and quantitative real-time polymerase chain reaction studies. *Human pathology* 54: 165-173

Kulkarni MM, Khandeparkar SG, Deshmukh SD, Karekar RR, Gaopande VL, Joshi AR, Kesari MV, Shelke RR (2016) Risk Stratification in Paragangliomas with PASS (Pheochromocytoma of the Adrenal Gland Scaled Score) and Immunohistochemical Markers. *Journal of clinical and diagnostic research : JCDR* 10: Ec01-ec04

Lam AK (2017) Update on Adrenal Tumours in 2017 World Health Organization (WHO) of

Endocrine Tumours. *Endocrine pathology* 28: 213-227

Lenders JW, Duh QY, Eisenhofer G, Gimenez-Roqueplo AP, Grebe SK, Murad MH, Naruse M, Pacak K, Young WF, Jr. (2014) Pheochromocytoma and paraganglioma: an endocrine society clinical practice guideline. *J Clin Endocrinol Metab* 99: 1915-1942

Lewis PD (1971) A cytophotometric study of benign and malignant phaeochromocytomas. *Virchows Arch B Cell Pathol* 9: 371-376

Li H, Durbin R (2009) Fast and accurate short read alignment with Burrows-Wheeler transform. *Bioinformatics (Oxford, England)* 25: 1754-1760

Li J, Byrne KT, Yan F, Yamazoe T, Chen Z, Baslan T, Richman LP, Lin JH, Sun YH, Rech AJ *et al* (2018) Tumor Cell-Intrinsic Factors Underlie Heterogeneity of Immune Cell Infiltration and Response to Immunotherapy. *Immunity* 49: 178-193.e177

Li PH, Kong XY, He YZ, Liu Y, Peng X, Li ZH, Xu H, Luo H, Park J (2022) Recent developments in application of single-cell RNA sequencing in the tumour immune microenvironment and cancer therapy. *Military Medical Research* 9: 52

Liang G, Liu Z, Wu J, Cai Y, Li X (2012) Anticancer molecules targeting fibroblast growth factor receptors. *Trends in pharmacological sciences* 33: 531-541

Liberzon A, Subramanian A, Pinchback R, Thorvaldsdóttir H, Tamayo P, Mesirov JP (2011) Molecular signatures database (MSigDB) 3.0. *Bioinformatics (Oxford, England)* 27: 1739-1740

Liu P, Li M, Guan X, Yu A, Xiao Q, Wang C, Hu Y, Zhu F, Yin H, Yi X *et al* (2018) Clinical Syndromes and Genetic Screening Strategies of Pheochromocytoma and Paraganglioma. *Journal of kidney cancer and VHL* 5: 14-22

Liu Y, Xun Z, Ma K, Liang S, Li X, Zhou S, Sun L, Liu Y, Du Y, Guo X *et al* (2023) Identification of a tumour immune barrier in the HCC microenvironment that determines the efficacy of immunotherapy. *Journal of hepatology* 78: 770-782

Liu Y, Zhang Q, Xing B, Luo N, Gao R, Yu K, Hu X, Bu Z, Peng J, Ren X *et al* (2022) Immune phenotypic linkage between colorectal cancer and liver metastasis. *Cancer cell* 40: 424-437.e425

Lupşan N, Resiga L, Boşca AB, Georgiu C, Crişan D, Mirescu C, Constantin AM, Şimon I,

Şovrea AS (2016) Diagnostic reevaluation of 17 cases of pheochromocytoma - a retrospective study. *Romanian journal of morphology and embryology = Revue roumaine de morphologie et embryologie* 57: 651-661

Mahmoodi N, Harijan RK, Schramm VL (2020) Transition-State Analogues of Phenylethanolamine N-Methyltransferase. *Journal of the American Chemical Society* 142: 14222-14233

McKenna A, Hanna M, Banks E, Sivachenko A, Cibulskis K, Kernytsky A, Garimella K, Altshuler D, Gabriel S, Daly M *et al* (2010) The Genome Analysis Toolkit: a MapReduce framework for analyzing next-generation DNA sequencing data. *Genome research* 20: 1297-1303

Mete O, Asa SL, Gill AJ, Kimura N, de Krijger RR, Tischler A (2022) Overview of the 2022 WHO Classification of Paragangliomas and Pheochromocytomas. *Endocrine pathology* 33: 90-114

Naing A, Meric-Bernstam F, Stephen B, Karp DD, Hajjar J, Rodon Ahnert J, Piha-Paul SA, Colen RR, Jimenez C, Raghav KP *et al* (2020) Phase 2 study of pembrolizumab in patients with advanced rare cancers. *Journal for immunotherapy of cancer* 8

Neumann HPH, Young WF, Jr., Eng C (2019) Pheochromocytoma and Paraganglioma. *The New England journal of medicine* 381: 552-565

Nölting S, Bechmann N, Taieb D, Beuschlein F, Fassnacht M, Kroiss M, Eisenhofer G, Grossman A, Pacak K (2022) Personalized Management of Pheochromocytoma and Paraganglioma. *Endocrine reviews* 43: 199-239

Nölting S, Grossman A, Pacak K (2019) Metastatic Phaeochromocytoma: Spinning Towards More Promising Treatment Options. *Experimental and clinical endocrinology & diabetes : official journal, German Society of Endocrinology [and] German Diabetes Association* 127: 117-128

O'Kane GM, Ezzat S, Joshua AM, Bourdeau I, Leibowitz-Amit R, Olney HJ, Krzyzanowska M, Reuther D, Chin S, Wang L *et al* (2019) A phase 2 trial of sunitinib in patients with progressive

paraganglioma or pheochromocytoma: the SNIPP trial. *British journal of cancer* 120: 1113-1119

Oh CY, Klatt MG, Bourne C, Dao T, Dacek MM, Brea EJ, Mun SS, Chang AY, Korontsvit T, Scheinberg DA (2019) ALK and RET Inhibitors Promote HLA Class I Antigen Presentation and Unmask New Antigens within the Tumor Immunopeptidome. *Cancer Immunol Res* 7: 1984-1997

Oh DY, Kim TW, Park YS, Shin SJ, Shin SH, Song EK, Lee HJ, Lee KW, Bang YJ (2012) Phase 2 study of everolimus monotherapy in patients with nonfunctioning neuroendocrine tumors or pheochromocytomas/paragangliomas. *Cancer* 118: 6162-6170

Papathomas TG, Suurd DPD, Pacak K, Tischler AS, Vriens MR, Lam AK, de Krijger RR (2021) What Have We Learned from Molecular Biology of Paragangliomas and Pheochromocytomas? *Endocrine pathology* 32: 134-153

Perea F, Sánchez-Palencia A, Gómez-Morales M, Bernal M, Concha Á, García MM, González-Ramírez AR, Kerick M, Martin J, Garrido F *et al* (2018) HLA class I loss and PD-L1 expression in lung cancer: impact on T-cell infiltration and immune escape. *Oncotarget* 9: 4120-4133

Pillai S, Gopalan V, Lam AK (2017) Review of sequencing platforms and their applications in phaeochromocytoma and paragangliomas. *Crit Rev Oncol Hematol* 116: 58-67

Powers JF, Brachold JM, Tischler AS (2003) Ret protein expression in adrenal medullary hyperplasia and pheochromocytoma. *Endocrine pathology* 14: 351-361

Powers JF, Picard KL, Tischler AS (2009) RET expression and neuron-like differentiation of pheochromocytoma and normal chromaffin cells. *Hormone and metabolic research = Hormon- und Stoffwechselforschung = Hormones et metabolisme* 41: 710-714

Ren X, Zhang L, Zhang Y, Li Z, Siemers N, Zhang Z (2021) Insights Gained from Single-Cell Analysis of Immune Cells in the Tumor Microenvironment. *Annual review of immunology* 39: 583-609

Roman-Gonzalez A, Jimenez C (2017) Malignant pheochromocytoma-paraganglioma: pathogenesis, TNM staging, and current clinical trials. *Current opinion in endocrinology, diabetes, and obesity* 24: 174-183

Sadagopan A, Michelakos T, Boyiadzis G, Ferrone C, Ferrone S (2022) Human Leukocyte

Antigen Class I Antigen-Processing Machinery Upregulation by Anticancer Therapies in the Era of Checkpoint Inhibitors: A Review. *JAMA oncology* 8: 462-473

Sade-Feldman M, Yizhak K, Bjorgaard SL, Ray JP, de Boer CG, Jenkins RW, Lieb DJ, Chen JH, Frederick DT, Barzily-Rokni M *et al* (2018) Defining T Cell States Associated with Response to Checkpoint Immunotherapy in Melanoma. *Cell* 175: 998-1013.e1020

Saelens W, Cannoodt R, Todorov H, Saeys Y (2019) A comparison of single-cell trajectory inference methods. *Nat Biotechnol* 37: 547-554

Sarkadi B, Saskoi E, Butz H, Patocs A (2022) Genetics of Pheochromocytomas and Paragangliomas Determine the Therapeutical Approach. *International journal of molecular sciences* 23

Satija R, Farrell JA, Gennert D, Schier AF, Regev A (2015) Spatial reconstruction of single-cell gene expression data. *Nat Biotechnol* 33: 495-502

Sherwin RP (1959) Histopathology of pheochromocytoma. *Cancer* 12: 861-877

Sinkler CA, Kalpage H, Shay J, Lee I, Malek MH, Grossman LI, Hüttemann M (2017) Tissue- and Condition-Specific Isoforms of Mammalian Cytochrome c Oxidase Subunits: From Function to Human Disease. *Oxidative medicine and cellular longevity* 2017: 1534056

Sisson JC, Shapiro B, Beierwaltes WH, Glowniak JV, Nakajo M, Mangner TJ, Carey JE, Swanson DP, Copp JE, Satterlee WG *et al* (1984) Radiopharmaceutical treatment of malignant pheochromocytoma. *J Nucl Med* 25: 197-206

Stanton SE, Disis ML (2016) Clinical significance of tumor-infiltrating lymphocytes in breast cancer. *Journal for immunotherapy of cancer* 4: 59

Stuart T, Butler A, Hoffman P, Hafemeister C, Papalexi E, Mauck WM, 3rd, Hao Y, Stoeckius M, Smibert P, Satija R (2019) Comprehensive Integration of Single-Cell Data. *Cell* 177: 1888-1902.e1821

Symington T, Goodall AL (1953) Studies in phaeochromocytoma. I. Pathological aspects. *Glasgow Med J* 34: 75-96

Thompson LD (2002) Pheochromocytoma of the Adrenal gland Scaled Score (PASS) to separate

benign from malignant neoplasms: a clinicopathologic and immunophenotypic study of 100 cases. *The American journal of surgical pathology* 26: 551-566

Toledo R, Jimenez C (2018) Recent advances in the management of malignant pheochromocytoma and paraganglioma: focus on tyrosine kinase and hypoxia-inducible factor inhibitors. *F1000Research* 7

Toledo RA, Burnichon N, Cascon A, Benn DE, Bayley JP, Welander J, Tops CM, Firth H, Dwight T, Ercolino T *et al* (2017) Consensus Statement on next-generation-sequencing-based diagnostic testing of hereditary phaeochromocytomas and paragangliomas. *Nature reviews Endocrinology* 13: 233-247

Tufton N, Hearnden RJ, Berney DM, Drake WM, Parvanta L, Chapple JP, Akker SA (2022) The immune cell infiltrate in the tumour microenvironment of phaeochromocytomas and paragangliomas. *Endocrine-related cancer* 29: 589-598

Vitale I, Shema E, Loi S, Galluzzi L (2021) Intratumoral heterogeneity in cancer progression and response to immunotherapy. *Nature medicine* 27: 212-224

Vortmeyer AO, Falke EA, Gläsker S, Li J, Oldfield EH (2013) Nervous system involvement in von Hippel-Lindau disease: pathology and mechanisms. *Acta Neuropathol* 125: 333-350

Wang K, Li M, Hakonarson H (2010) ANNOVAR: functional annotation of genetic variants from high-throughput sequencing data. *Nucleic acids research* 38: e164

Wiedenmann B, Waldherr R, Buhr H, Hille A, Rosa P, Huttner WB (1988) Identification of gastroenteropancreatic neuroendocrine cells in normal and neoplastic human tissue with antibodies against synaptophysin, chromogranin A, secretogranin I (chromogranin B), and secretogranin II. *Gastroenterology* 95: 1364-1374

Winkler H, Fischer-Colbrie R (1992) The chromogranins A and B: the first 25 years and future perspectives. *Neuroscience* 49: 497-528

Wu D, Tischler AS, Lloyd RV, DeLellis RA, de Krijger R, van Nederveen F, Nosé V (2009) Observer variation in the application of the Pheochromocytoma of the Adrenal Gland Scaled Score. *The American journal of surgical pathology* 33: 599-608

Yates R, Katugampola H, Cavlan D, Cogger K, Meimaridou E, Hughes C, Metherell L, Guasti L, King P (2013) Adrenocortical development, maintenance, and disease. *Current topics in developmental biology* 106: 239-312

Yu G, Wang LG, Han Y, He QY (2012) clusterProfiler: an R package for comparing biological themes among gene clusters. *Omics* 16: 284-287

Zhang X, Lan Y, Xu J, Quan F, Zhao E, Deng C, Luo T, Xu L, Liao G, Yan M *et al* (2019) CellMarker: a manually curated resource of cell markers in human and mouse. *Nucleic acids research* 47: D721-d728

Zhang Y, Yao Y, Chen P, Liu Y, Zhang H, Liu H, Liu Y, Xu H, Tian X, Wang Z *et al* (2020) Checkpoint therapeutic target database (CKTTD): the first comprehensive database for checkpoint targets and their modulators in cancer immunotherapy. *Journal for immunotherapy of cancer* 8

Zhang Y, Zhang Z (2020) The history and advances in cancer immunotherapy: understanding the characteristics of tumor-infiltrating immune cells and their therapeutic implications. *Cellular & molecular immunology* 17: 807-821

FIGURE LEGENDS

Figure 1. Integration Analysis across 5 PCC Patients Revealing the Cell Composition of the PCC Microenvironment. (A) Schematic of the experimental pipeline. 11 tumor specimens and 5 adjacent normal adrenal medullary specimens were isolated from 5 PCC patients, dissociated into single-cell suspensions, and analyzed using 10x Genomics Chromium droplet scRNA-seq. (B) UMAP plots illustrating 133,894 cells from 16 specimens across 5 PCC patients. Cells color-coded by specimens, patients, and tissue types. (C) UMAP plot showing 13 main cell types from all specimens. (D) Dot plot of representative marker genes for each cell type. The color scale represents the average marker gene expression level; dot size represents the percentage of cells expressing a given marker gene.

Figure 2. Correlation Analysis Reveals Less intra-tumoral Heterogeneity than inter-individual Heterogeneity. (A) Heatmap plotting the correlation coefficient among 16 specimens. The color keys from blue to red indicate the correlation coefficient from low to high. (B) Bar plot showing the percentage of cell types in 16 specimens. (C) Heatmap of the correlation coefficient among 5 PCC patients. The color keys from blue to red indicate the correlation coefficient from low to high. (D) Bar plot depicting the frequency distribution of cell types in 5 PCC patients.

Figure 3. Single-cell Copy Number Profiles in PCC Clusters Inferred by CopyKAT. (A)

Heatmap indicating the CNV patterns of inferred normal cells, tumor cells, tumor cluster A, and tumor cluster B. Blue, white, and red respectively indicate deletion from a chromosome, normal chromosome, and amplification on a chromosome. (B) UMAP plot of the inferred normal cells (blue) and tumor cells (red) identified by CopyKAT. (C) Feature plots showing the marker gene expression levels in inferred normal cells and tumor cells. (D) UMAP plot depicting the inferred normal cells (blue), tumor cluster A (purple), and tumor cluster B (orange) identified by CopyKAT. (E) Feature plots displaying the marker gene expression levels in inferred tumor cluster A and B.

Figure 4. PCC Patients were Classified into Metabolism-type and Kinase-type. (A) Heatmap plotting the scaled expression patterns of major marker genes in each tumor cluster. The color keys from pink to yellow indicate relative expression levels from low to high. (B) Dot plot depicting up-regulated genes of tumor cluster A (top) and tumor cluster B (bottom). The x-axis specifies the rank of DEGs and the y-axis specifies the natural logarithm of the FC. Dotted vertical and horizontal lines reflect the filtering criteria. Dot size represents the natural logarithm of the FC of genes. The color keys from blue to red indicate the P-value from high to low. (C, D) GO enrichment analysis of the up-regulated genes in tumor cluster A (C) and tumor cluster B (D) indicating the top altered 10 terms in the biological process of gene ontology. The x-axis specifies the number of genes enriched in the pathways. The color keys from shallow to deep indicate the P-value from high to low. (E) Immunohistochemistry staining of CGA, NDUFA4L2, COX4I2, PNMT, and RET markers in formalin-fixed paraffin-embedded PCC tissue sections matched to

scRNA-seq specimens. Scale bar, 100 μm.

Figure 5. Pseudotime Analysis of PCC Tumor Evolution by Dynverse. (A, B) Pseudotime trajectory of metabolism-type PCC cells colored by pseudotime (A) and tumor subclusters (B). (C) Pseudotime heatmap plotting the expression levels of genes across the transition from beginning (left) to end (right). The color keys from blue to red indicate the gene expression levels from low to high. (D, E) Pseudotime trajectory of kinase-type PCC cells colored by pseudotime (D) and tumor subclusters (E). (F) Pseudotime heatmap showing the expression levels of genes across the transition from beginning (left) to end (right). The color keys from blue to red indicate the gene expression levels from low to high.

Figure 6. CellChat Analysis Reveals Cell-cell Communication Patterns in PCC Types. (A) Circle plot showing an inferred annexin signaling pathway network in the metabolism-type PCC microenvironment. The edges connecting the circles represent the communication probability between any two kinds of cell types. The color of the edge denotes directionality (i.e., senders *vs* receivers). (B) Bar graph plotting the quantification of the relative contributions of individual ligand-receptor pairs to the overall annexin signaling pathway. (C) Violin plot of the expression distribution of *ANXA1*, *FPR1*, and *FPR2* in main cell types of the metabolism-type PCC microenvironment. (D) GSEA enrichment plots of the inflammatory response signaling of metabolism-type patients (left) and the kinase-type patient (right). (E) Circle plot depicting an inferred VEGF signaling pathway. (F) Bar graph displaying the quantification of the relative

contributions of individual ligand-receptor pairs to the overall VEGF communication network. (G) Violin plot plotting the expression distribution of *VEGFA*, *VEGFB*, *PLGF*, *VEGFR1*, and *VEGFR2* in main cell types of P5 PCC microenvironment. (H) Circle plot of an inferred FGF signaling pathway in the kinase-type PCC microenvironment. (I) Bar graph showing the quantification of the relative contributions of individual ligand-receptor pairs to the overall FGF signaling pathway. (J) Violin plot plotting the expression distribution of *FGF1*, *FGF18*, and *FGFR1* in main cell types of the kinase-type PCC microenvironment.

Figure 7. Prediction of the Immune Escape Potential and Immunotherapy Response of PCC Patients. (A) Circle plots depicting inferred inter-cellular interactions in metabolism-type (left) and kinase-type (right) PCC microenvironment. (B) Box plots showing the expression levels of *HLA-A*, *HLA-B*, and *HLA-C* in metabolism-type and kinase-type PCC patients. (C) Immunohistochemistry staining of CGA and HLA-A in formalin-fixed paraffin-embedded PCC tissue sections matched to scRNA-seq specimens. Scale bar, 100 μm. (D) UMAP plot showing 8 immune cell types detected from all PCC specimens. (E) Dot plot of representative marker genes for each immune cell type. The color scale represents the average marker gene expression level; dot size represents the percentage of cells expressing a given marker gene. (F) Comparison of the proportion of immune cell types in tumor *vs* adjacent normal adrenal medullary tissues. (G) Multispectral immunofluorescent staining for the juxtaposition of PCC cells (marked by CGA), $CD4^+$ T cells (marked by CD4), $CD8^+$ T cells (marked by CD8), M1 macrophages (marked by CD68), and M2 macrophages (marked by CD163) in formalin-fixed

paraffin-embedded PCC tissue sections matched to scRNA-seq specimens. The white, yellow, cyan, green, pink, and blue spots indicated cells with high expression of CGA, CD4, CD8, CD68, CD163, and DAPI proteins in PCC tissue sections, respectively. S, stroma; T, tumor. Scale bar, 100 μm.

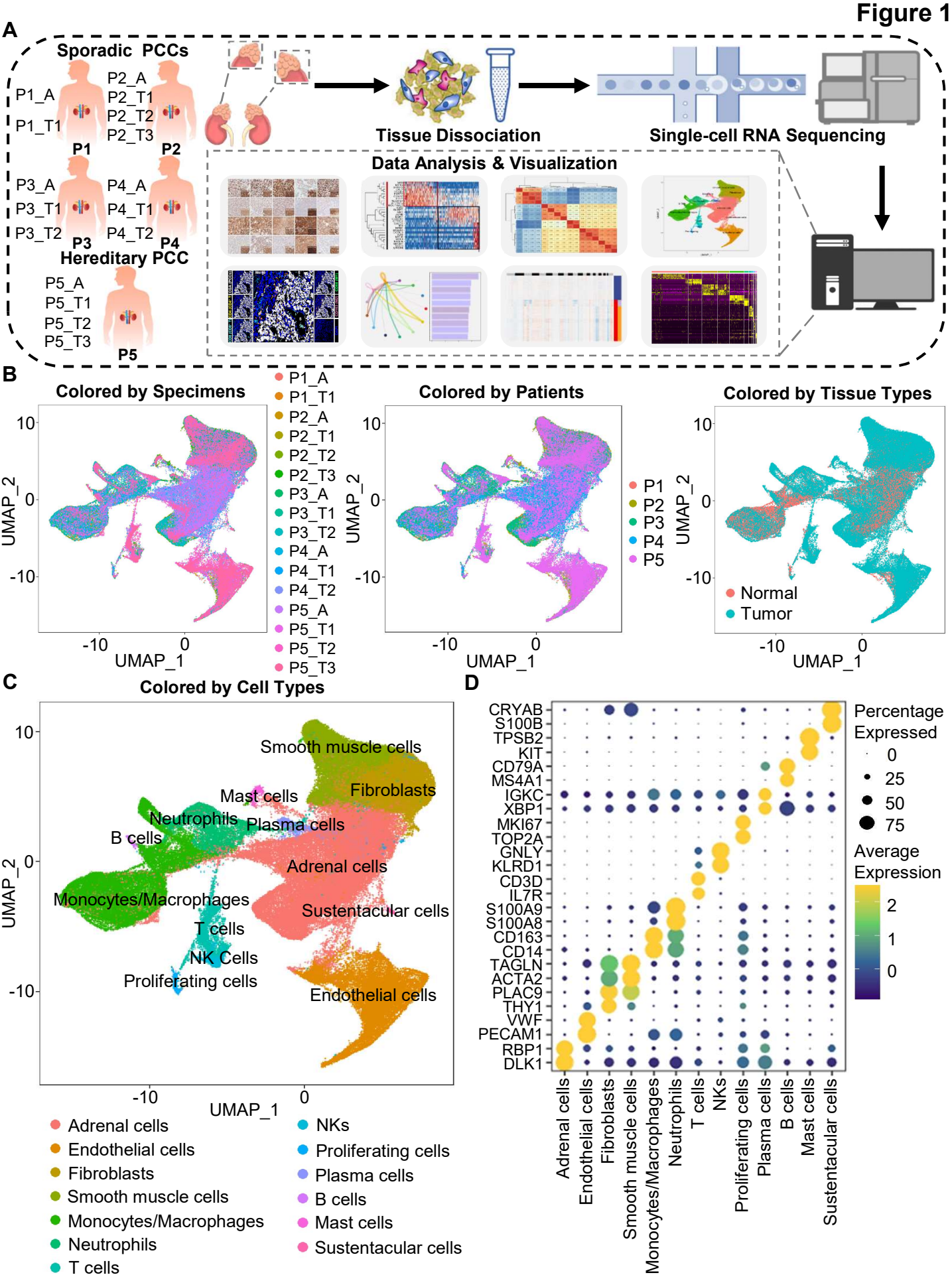
Figure 1
A
Sporadic PCCs
P1_A
P1_T1
P1
P2_A
P2_T1
P2_T2
P2_T3
P2
P3_A
P3_T1
P3_T2
P3
P4_A
P4_T1
P4_T2
P4
Hereditary PCC
P5_A
P5_T1
P5_T2
P5_T3
P5
Tissue Dissociation
Single-cell RNA Sequencing
Data Analysis & Visualization
B
Colored by Specimens
Colored by Patients
Colored by Tissue Types
UMAP_1
UMAP_2
P1_A
P1_T1
P2_A
P2_T1
P2_T2
P2_T3
P3_A
P3_T1
P3_T2
P4_A
P4_T1
P4_T2
P5_A
P5_T1
P5_T2
P5_T3
P1
P2
P3
P4
P5
Normal
Tumor
C
Colored by Cell Types
Smooth muscle cells
Fibroblasts
Mast cells
Neutrophils
Plasma cells
B cells
Adrenal cells
Monocytes/Macrophages
Sustentacular cells
T cells
NK Cells
Proliferating cells
Endothelial cells
Adrenal cells
Endothelial cells
Fibroblasts
Smooth muscle cells
Monocytes/Macrophages
Neutrophils
T cells
NKs
Proliferating cells
Plasma cells
B cells
Mast cells
Sustentacular cells
D
CRYAB
S100B
TPSB2
KIT
CD79A
MS4A1
IGKC
XBP1
MKI67
TOP2A
GNLY
KLRD1
CD3D
IL7R
S100A9
S100A8
CD163
CD14
TAGLN
ACTA2
PLAC9
THY1
VWF
PECAM1
RBP1
DLK1
Percentage Expressed
0
25
50
75
Average Expression
2
1
0

Figure 2

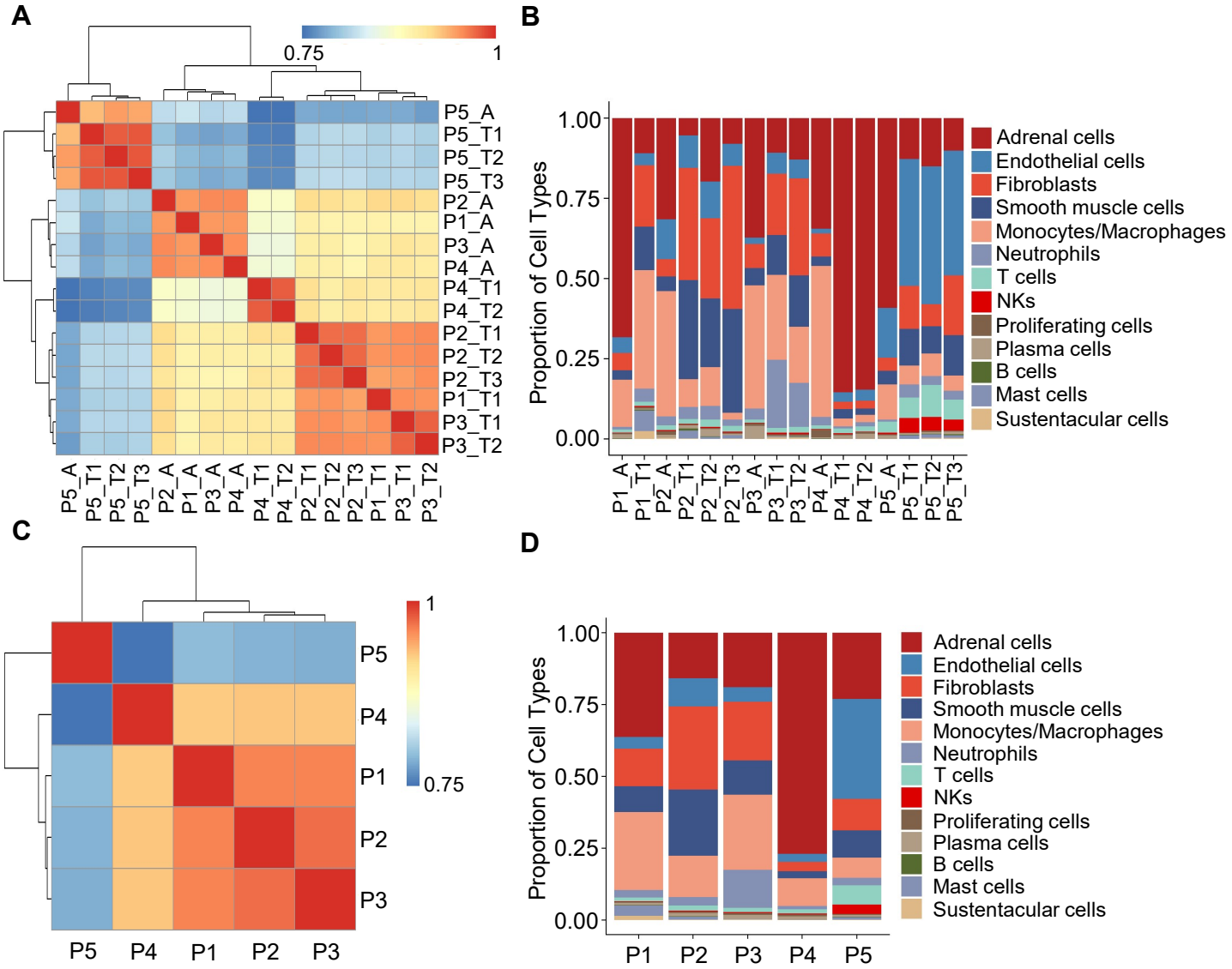
A
0.75
1
P5_A
P5_T1
P5_T2
P5_T3
P2_A
P1_A
P3_A
P4_A
P4_T1
P4_T2
P2_T1
P2_T2
P2_T3
P1_T1
P3_T1
P3_T2
B
Proportion of Cell Types
1.00
0.75
0.50
0.25
0.00
Adrenal cells
Endothelial cells
Fibroblasts
Smooth muscle cells
Monocytes/Macrophages
Neutrophils
T cells
NKs
Proliferating cells
Plasma cells
B cells
Mast cells
Sustentacular cells
C
1
0.75
P5
P4
P1
P2
P3
D
Proportion of Cell Types
1.00
0.75
0.50
0.25
0.00
P1
P2
P3
P4
P5

Figure 3

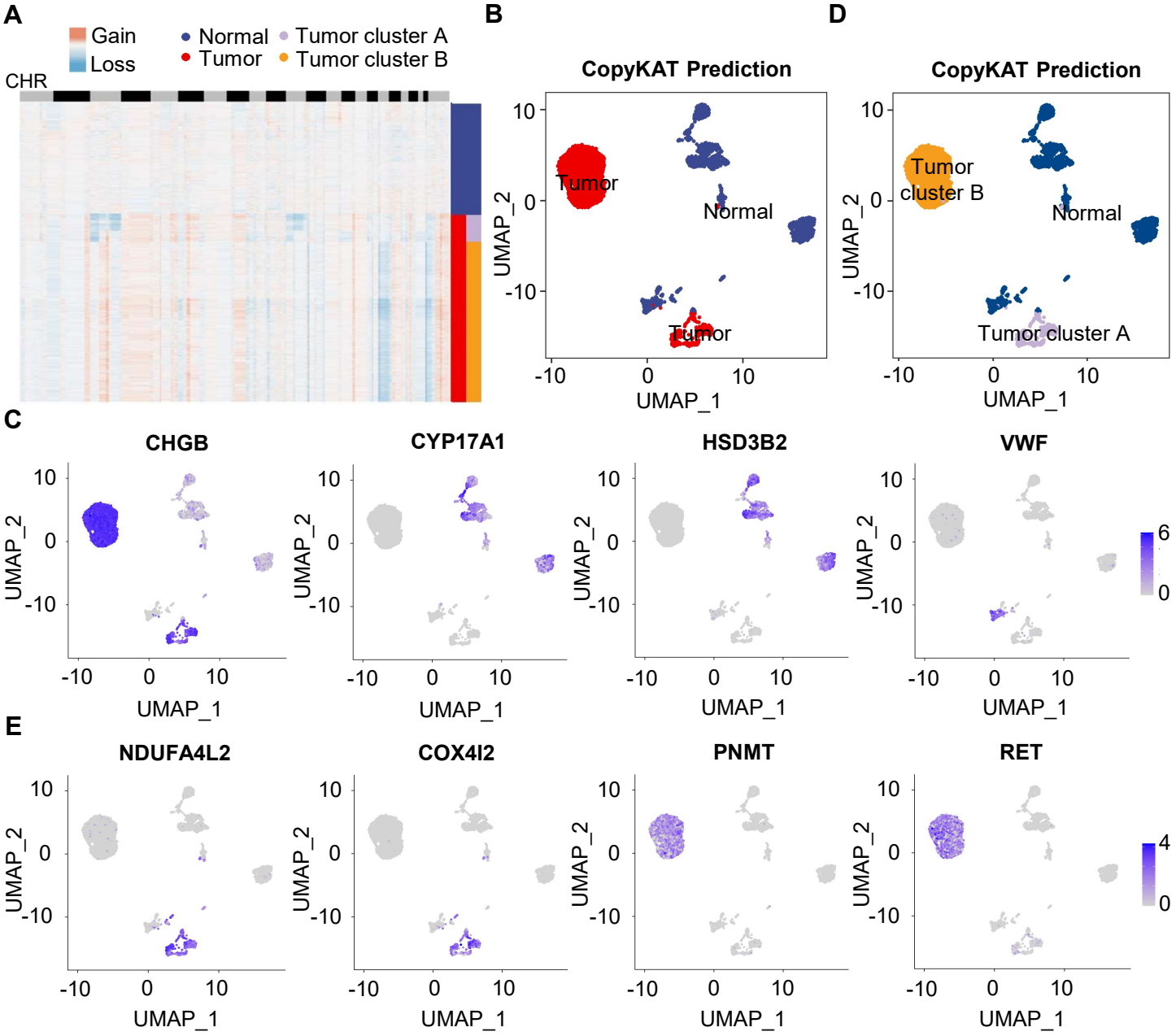
A
Gain
Loss
CHR
Normal
Tumor
Tumor cluster A
Tumor cluster B
B
CopyKAT Prediction
Tumor
Normal
Tumor
UMAP_2
UMAP_1
D
CopyKAT Prediction
Tumor cluster B
Normal
Tumor cluster A
C
CHGB
CYP17A1
HSD3B2
VWF
6
0
E
NDUFA4L2
COX4I2
PNMT
RET
4
0

Figure 4

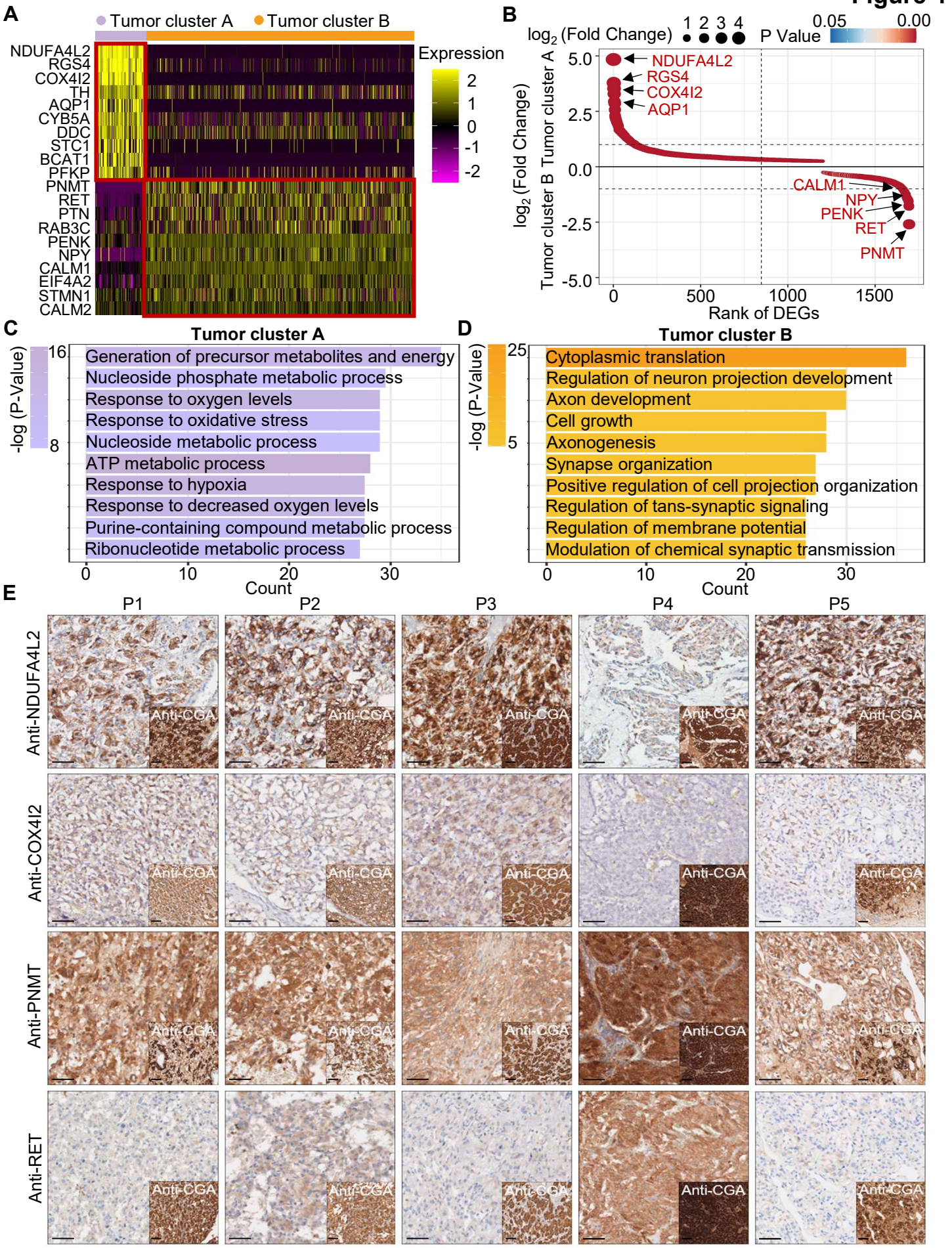
A
Tumor cluster A
Tumor cluster B
NDUFA4L2
RGS4
COX4I2
TH
AQP1
CYB5A
DDC
STC1
BCAT1
PFKP
PNMT
RET
PTN
RAB3C
PENK
NPY
CALM1
EIF4A2
STMN1
CALM2
Expression
2
1
0
-1
-2
B
log2 (Fold Change)
1 2 3 4
P Value
0.05
0.00
Tumor cluster B Tumor cluster A
log2 (Fold Change)
5.0
2.5
0.0
-2.5
-5.0
NDUFA4L2
RGS4
COX4I2
AQP1
CALM1
NPY
PENK
RET
PNMT
0
500
1000
1500
Rank of DEGs
C
Tumor cluster A
-log (P-Value)
16
8
Generation of precursor metabolites and energy
Nucleoside phosphate metabolic process
Response to oxygen levels
Response to oxidative stress
Nucleoside metabolic process
ATP metabolic process
Response to hypoxia
Response to decreased oxygen levels
Purine-containing compound metabolic process
Ribonucleotide metabolic process
0
10
20
30
Count
D
Tumor cluster B
-log (P-Value)
25
5
Cytoplasmic translation
Regulation of neuron projection development
Axon development
Cell growth
Axonogenesis
Synapse organization
Positive regulation of cell projection organization
Regulation of tans-synaptic signaling
Regulation of membrane potential
Modulation of chemical synaptic transmission
0
10
20
30
Count
E
P1
P2
P3
P4
P5
Anti-NDUFA4L2
Anti-COX4I2
Anti-PNMT
Anti-RET
Anti-CGA

Figure 5

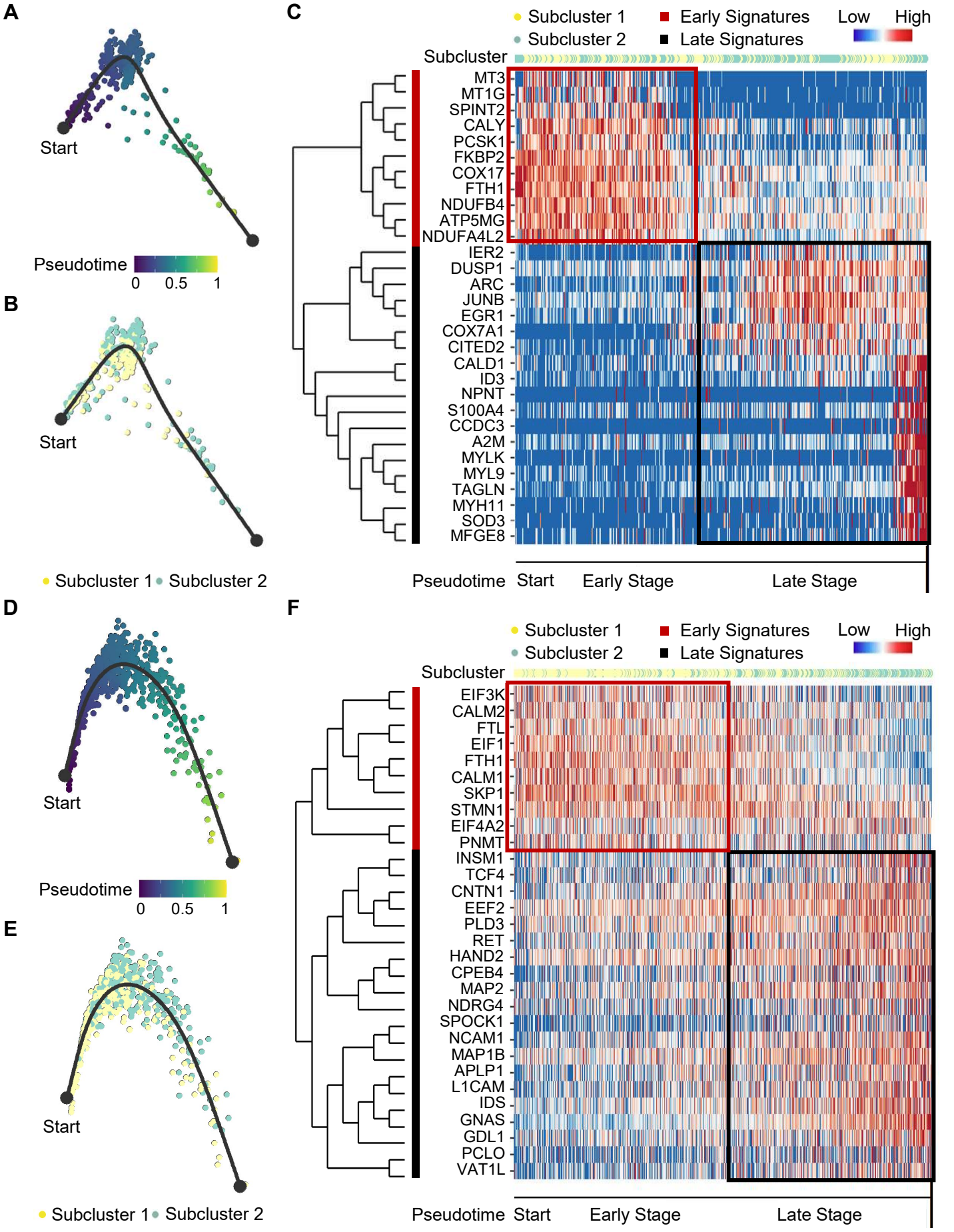
A
Start
Pseudotime
0
0.5
1
B
Start
Subcluster 1
Subcluster 2
C
Subcluster 1
Subcluster 2
Early Signatures
Late Signatures
Low
High
Subcluster
MT3
MT1G
SPINT2
CALY
PCSK1
FKBP2
COX17
FTH1
NDUFB4
ATP5MG
NDUFA4L2
IER2
DUSP1
ARC
JUNB
EGR1
COX7A1
CITED2
CALD1
ID3
NPNT
S100A4
CCDC3
A2M
MYLK
MYL9
TAGLN
MYH11
SOD3
MFGE8
Pseudotime
Start
Early Stage
Late Stage
D
Start
Pseudotime
0
0.5
1
E
Start
Subcluster 1
Subcluster 2
F
Subcluster 1
Subcluster 2
Early Signatures
Late Signatures
Low
High
Subcluster
EIF3K
CALM2
FTL
EIF1
FTH1
CALM1
SKP1
STMN1
EIF4A2
PNMT
INSM1
TCF4
CNTN1
EEF2
PLD3
RET
HAND2
CPEB4
MAP2
NDRG4
SPOCK1
NCAM1
MAP1B
APLP1
L1CAM
IDS
GNAS
GDL1
PCLO
VAT1L
Pseudotime
Start
Early Stage
Late Stage

Figure 6

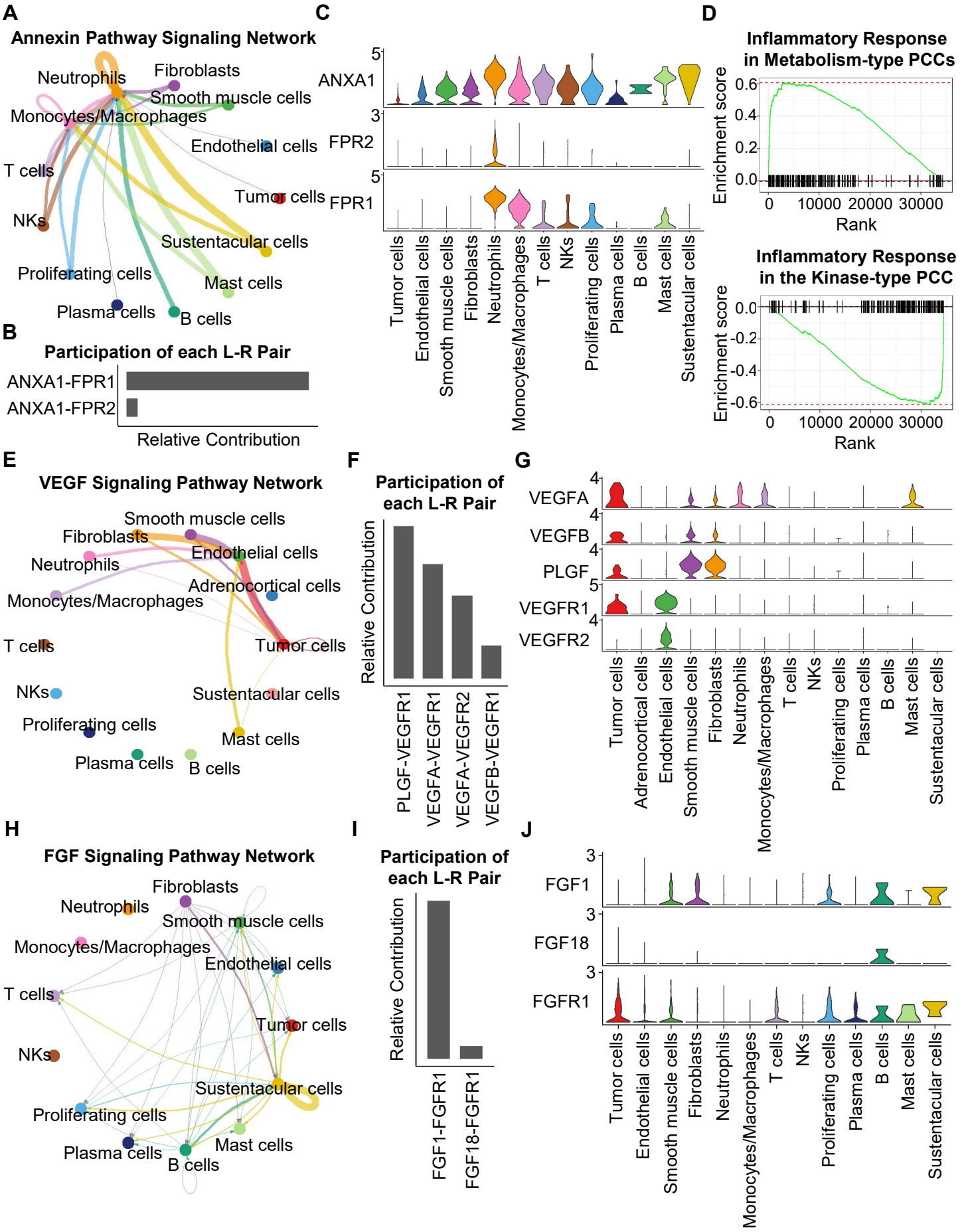
A
Annexin Pathway Signaling Network
Neutrophils
Fibroblasts
Smooth muscle cells
Monocytes/Macrophages
Endothelial cells
T cells
Tumor cells
NKs
Sustentacular cells
Proliferating cells
Mast cells
Plasma cells
B cells
B
Participation of each L-R Pair
ANXA1-FPR1
ANXA1-FPR2
Relative Contribution
C
ANXA1
FPR2
FPR1
Tumor cells
Endothelial cells
Smooth muscle cells
Fibroblasts
Neutrophils
Monocytes/Macrophages
T cells
NKs
Proliferating cells
Plasma cells
B cells
Mast cells
Sustentacular cells
D
Inflammatory Response in Metabolism-type PCCs
Enrichment score
Rank
Inflammatory Response in the Kinase-type PCC
Enrichment score
Rank
E
VEGF Signaling Pathway Network
Smooth muscle cells
Fibroblasts
Endothelial cells
Neutrophils
Adrenocortical cells
Monocytes/Macrophages
T cells
Tumor cells
NKs
Sustentacular cells
Proliferating cells
Mast cells
Plasma cells
B cells
F
Participation of each L-R Pair
Relative Contribution
PLGF-VEGFR1
VEGFA-VEGFR1
VEGFA-VEGFR2
VEGFB-VEGFR1
G
VEGFA
VEGFB
PLGF
VEGFR1
VEGFR2
Tumor cells
Adrenocortical cells
Endothelial cells
Smooth muscle cells
Fibroblasts
Neutrophils
Monocytes/Macrophages
T cells
NKs
Proliferating cells
Plasma cells
B cells
Mast cells
Sustentacular cells
H
FGF Signaling Pathway Network
Fibroblasts
Neutrophils
Smooth muscle cells
Monocytes/Macrophages
Endothelial cells
T cells
Tumor cells
NKs
Sustentacular cells
Proliferating cells
Mast cells
Plasma cells
B cells
I
Participation of each L-R Pair
Relative Contribution
FGF1-FGFR1
FGF18-FGFR1
J
FGF1
FGF18
FGFR1
Tumor cells
Endothelial cells
Smooth muscle cells
Fibroblasts
Neutrophils
Monocytes/Macrophages
T cells
NKs
Proliferating cells
Plasma cells
B cells
Mast cells
Sustentacular cells

Figure 7

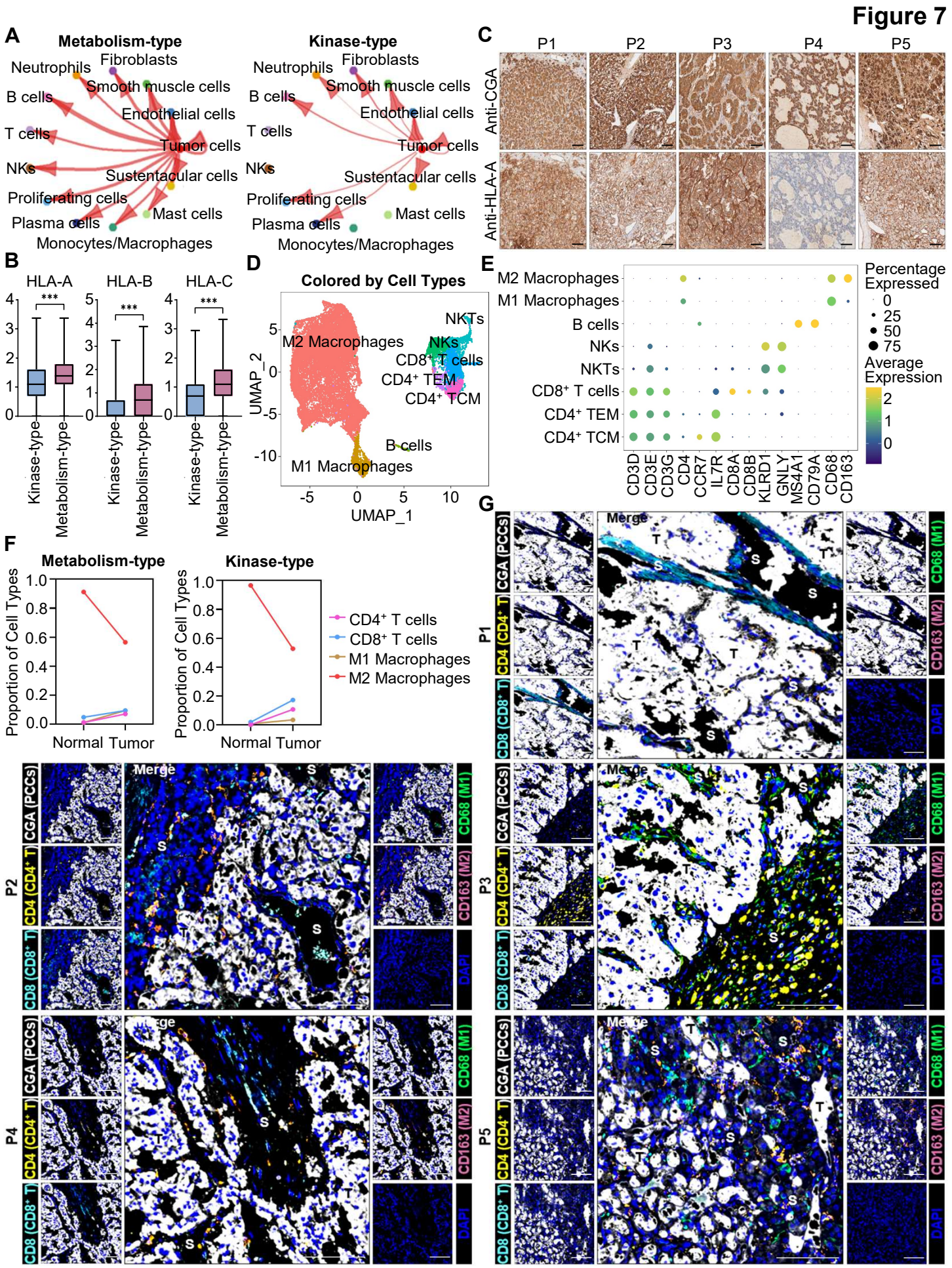

A
Metabolism-type
Kinase-type
Neutrophils
Fibroblasts
Smooth muscle cells
B cells
Endothelial cells
T cells
Tumor cells
NKs
Sustentacular cells
Proliferating cells
Mast cells
Plasma cells
Monocytes/Macrophages
B
HLA-A
HLA-B
HLA-C
***
Kinase-type
Metabolism-type
C
P1
P2
P3
P4
P5
Anti-CGA
Anti-HLA-A
D
Colored by Cell Types
NKTs
M2 Macrophages
NKs
CD8⁺ T cells
CD4⁺ TEM
CD4⁺ TCM
B cells
M1 Macrophages
UMAP_1
UMAP_2
E
M2 Macrophages
M1 Macrophages
B cells
NKs
NKTs
CD8⁺ T cells
CD4⁺ TEM
CD4⁺ TCM
CD3D
CD3E
CD3G
CD4
CCR7
IL7R
CD8A
CD8B
KLRD1
GNLY
MS4A1
CD79A
CD68
CD163
Percentage Expressed
0
25
50
75
Average Expression
2
1
0
F
Metabolism-type
Kinase-type
Proportion of Cell Types
Normal
Tumor
CD4⁺ T cells
CD8⁺ T cells
M1 Macrophages
M2 Macrophages
G
P1
P2
P3
P4
P5
Merge
CGA (PCCs)
CD4 (CD4⁺ T)
CD8 (CD8⁺ T)
CD68 (M1)
CD163 (M2)
DAPI